

CONSTRAINING THE HIGH DENSITY NUCLEAR SYMMETRY ENERGY WITH PIONS

By

Justin Estee

A DISSERTATION

Submitted
to Michigan State University
in partial fulfillment of the requirements
for the degree of

Physics – Doctor of Philosophy

2020

ABSTRACT

CONSTRAINING THE HIGH DENSITY NUCLEAR SYMMETRY ENERGY WITH PIONS

By

Justin Estee

Copyright by
JUSTIN ESTEE
2020

ACKNOWLEDGEMENTS

Your acknowledgements here.

TABLE OF CONTENTS

LIST OF TABLES	vii
LIST OF FIGURES	viii
CHAPTER 1 DATA ANALYSIS I: CALIBRATION AND CORRECTIONS	1
1.1 S π RITROOT Software	1
1.1.1 Decoder task	1
1.1.2 Pulse Shape Algorithm (PSA) Task	1
1.1.3 Vertex	2
1.1.4 Pulse Shape Algorithm	5
1.2 Corrections Task	5
1.2.1 Pad response function cut	5
1.3 Calibrations and Corrections	5
1.3.1 Gating grid noise subtraction	5
1.3.2 Cocktail calibration	7
1.3.3 Electronics calibration	9
1.3.4 Anode gain calibration	10
1.3.5 Extending the dynamic range of the Electronics	12
1.3.6 Experimental Pad Response Function	14
1.3.7 Method of Desaturation	15
1.3.8 Space Charge Corrections	20
1.4 Monte Carlo Simulation	28
1.4.1 Drift Task	30
1.4.2 Pad Response Task	32
1.4.3 Electronics Task	33
1.4.4 Simulating Saturation	34
1.5 Monte Carlo Track Embedding	39
1.5.1 MC and Data Comparison	44
1.6 Aligning TPC	45
1.7 CoBo timing correction	45
1.8 Efficiency Corrections	46
CHAPTER 2 DATA ANALYSIS II	52
2.1 Radio Isotope Beam Factory (RIBF) Facility	52
2.2 Beam Particle Identification	53
2.3 Edge Cuts	56
2.4 High Density Cut	57
2.5 Beam angle selection	57
2.6 Vertex Cut	59
2.7 Impact Parameter Selection	62
2.8 Track Quality Cuts	63

2.9 Angular Quality Cuts	65
APPENDIX	68
BIBLIOGRAPHY	71

LIST OF TABLES

Table 1.1	Summary of expected cocktail.	7
Table 1.2	Summary of expected cocktail.	7
Table 1.3	Summary of expected cocktail.	7
Table 1.4	Summary of expected cocktail.	9
Table 1.5	An overview of the properties of the TPC	31
Table 2.1	Primary and secondary beam properties produced in the S π RIT TPC experimental campaigns.	53
Table 2.2	Multivariate normal distribution fit parameters for four beams.	55
Table 2.3	2D Gaussian fit parameters for ^{132}Sn , ^{112}Sn and ^{108}Sn beam angle.	58
Table 2.4	Summary of measured vertexes and their resolution.	60
Table 2.5	Angular cuts for each system and particle type	65
Table .1	List of runs for the analysis.	69

LIST OF FIGURES

Figure 1.1 Example of the pulse shape algorithm through each step of in processing a given pad.	2
Figure 1.2 Cartoon graphic of a top down view of a fit to a track passing through several pads. The bolded pads and the charges q_i represent the hits belonging to that pad and the clusters of the track representing the average position of the track. The three clusters at the bottom are clustered in the x-direction and for the upper three clustered in the z-direction. The estimate of the position of the avalanche is given by the track fit and the position from the center to each pad to the \bar{x} position is given as λ_i	4
Figure 1.3 Gating grid noise profile and subtraction for a particular pad.	6
Figure 1.4 Calibration of electronics	10
Figure 1.5 Calibration of low high.	11
Figure 1.6 The expected dE/dx lines of different particles are given in red as calculated by Geant4. The approximate dynamic range of the TPC is shown by the vertical bar for the gain setting used in the experiment. Anything outside of this region would be saturated to some degree.	14
Figure 1.7 PRF response from π^- data.	16
Figure 1.8 Parameters N_0 and σ as a function of the crossing angle θ with the 4 th order polynomial fits.	17
Figure 1.9 A typical case of a saturating event. The red pulses represent the time bucket signal for each collected charge. The pads directly underneath the avalanche point, q_2' and q_3' , are saturated while pads farther away, q_1 and q_4 are not saturated.	18
Figure 1.10 Uncorrected (left panel) and desaturated (right panel) collision data at polar angles of $\theta < 40^\circ$ and azimuthal angles between $-80^\circ < \phi < 80^\circ$	19
Figure 1.11 Location of space charge in 132 Sn	21
Figure 1.12 Beam path of the experiments	22
Figure 1.13 Shift of tracks	24
Figure 1.14 ΔV_x distribution for left-going and right-going tracks in the TPC for the	25

Figure 1.15 ΔV_{LR} versus the beam rate for all systems with the fitted function.	26
Figure 1.16 Space charge fit function versus the beam rate for all systems. These are the assumed functions we use for interpolating the space charge value from the beam rate.	27
Figure 1.17 Space charge relation	28
Figure 1.18 Distribution of estimated space charge densities for each beam type.	29
Figure 1.19 Residuals in the fitted line of ΔV_{LR} observable for all systems.	29
Figure 1.21 Standard pulse	34
Figure 1.22 Pole zero correction	36
Figure 1.23 Geant4 simulation of ^{108}Sn beam at 270 MeV/A in P10 gas. Notice the extent of the delta electrons in the vertical direction as compared to the horizontal extent.	37
Figure 1.24 Tagging the saturated pads.	37
Figure 1.25 Flow of embedding implementation in the software.	40
Figure 1.26 A 200 MeV/c π^- embedded into a nuclear collision type event. The embedded track identified by the software is highlighted by the solid green line.	41
Figure 1.27 A 200 MeV/c π^- embedded into a nuclear collision type event. The embedded track identified by the software is highlighted by the solid green line.	42
Figure 1.28 Comparison of MC to data.	45
Figure 1.29 Comparison of MC to data.	46
Figure 1.30 PRF response of Monte Carlo simulation of π^-	47
Figure 1.31 TBW	48
Figure 1.32	49
Figure 1.33 Efficiency calculations for π^- particle traveling at $200 \text{ MeV } c^{-1}$	50
Figure 1.34	51
Figure 1.35	51
Figure 2.1 Overview of the RIBF, BigRIPS, and SAMURAI beamline.	52

Figure 2.2	Overall beam PID for all the systems. Several contaminants other than the desired secondary beam can be seen.	54
Figure 2.3	$^{108}\text{Sn} + ^{112}\text{Sn}$ Beam particle identification.	54
Figure 2.4		56
Figure 2.5	Views showing the high density and edge cuts.	57
Figure 2.7	Projection of the vertex onto the z-axis.	59
Figure 2.8		61
Figure 2.9	Estimate of the impact parameter from the track multiplicity.	62
Figure 2.10	Distance to vertex for tracks.	64
Figure 2.11	Rough Geometry of the TPC field cage.	66
Figure 2.12	Three simple graphs	66
Figure 2.13	Three simple graphs	66

CHAPTER 1

DATA ANALYSIS I: CALIBRATION AND CORRECTIONS

1.1 S π RITROOT Software

The S π RITROOT software is modular task based code based on the FAIRROOT package written in C++ [1]. The main tasks in the S π RITROOT software reconstruction are:

- Decoder task
- Pulse Shape Algorithm (PSA Task)
- Helix Track Finding Algorithm
- Clustering Algorithm
- Track Fitting (GENFIT package)
- Vertex Fitting (RAVE package)

1.1.1 Decoder task

The decoder task converts the binary data file into a container class which maps the electronics channels into the corresponding pads and (x,z) coordinates.

1.1.2 Pulse Shape Algorithm (PSA) Task

There may be several pulses in a pad coming from two tracks passing under the same pad separated by arrival time. Using an expected pulse shape the PSA task fits the signal pulses within a pad, giving the arrival time of the drifted electrons from each particular track. The height of the fitted pulse is proportional to the total charge of that event, Q and the y-coordinate is calculated as $y = v \cdot t_0$ where v is the drift velocity and t_0 the arrival time. Combining the information from these first two tasks, (x,y,z,Q), we construct what is called a "hit".

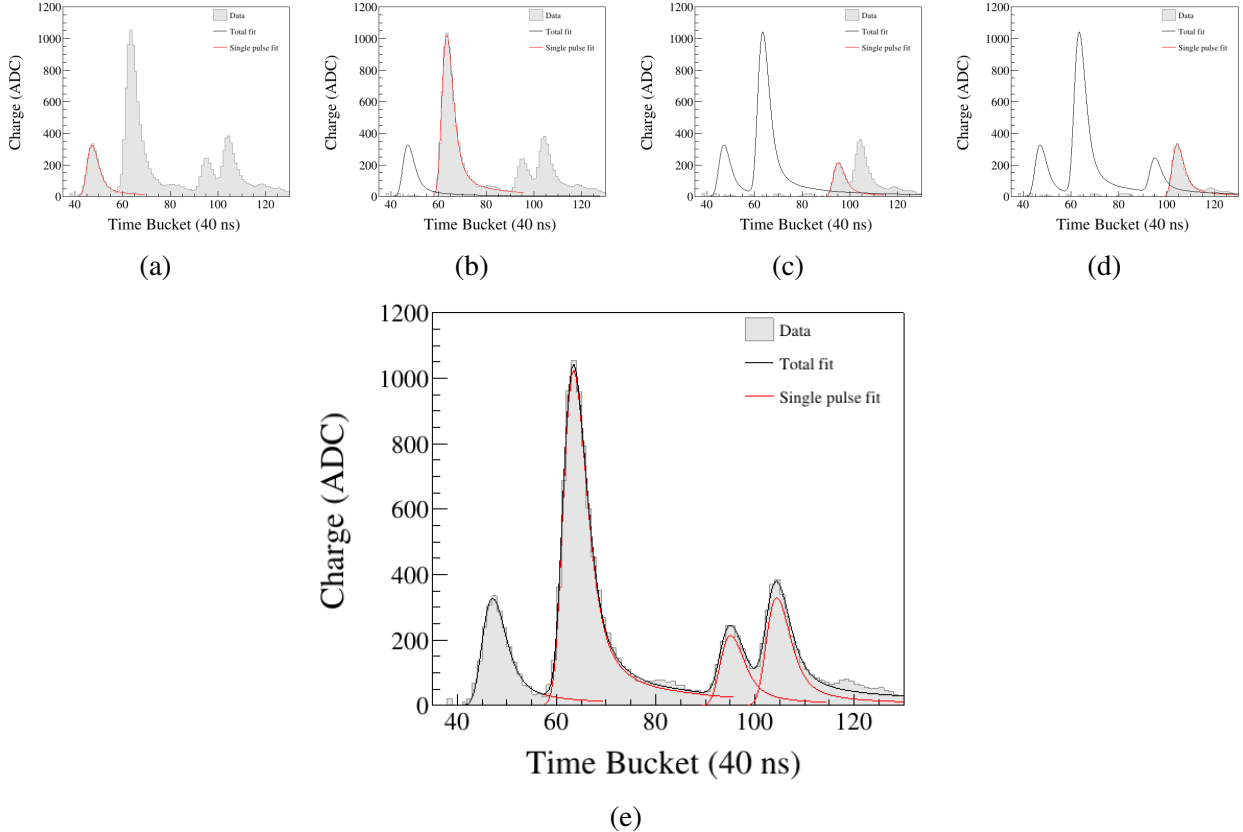


Figure 1.1: Example of the pulse shape algorithm through each step of in processing a given pad.

The Helix Track Finding Algorithm finds the collection of hits belonging to one track out of all the hits in an event. The hits within a track are then reduced into clusters. A cluster's position is the average position of the hits within a cluster, with the total charge of the cluster being the sum of the hits charges.

A tracks average position is estimated by the cluster's average position. The clusters are then fitted in the GENFIT track fitting package [2], giving the final momentum of the track. A final vertex of the event is fitted from all tracks using the package RAVE [3].

1.1.3 Vertex

Definition of clustering A brief description of the method of clustering is illustrated in Figure 1.2. It is impractical to cluster in both the x and z-axis and we only cluster the hits along one axis. The three clusters at the bottom of Figure 1.2 are clustered along the x-axis and the upper three are

along the z-axis, as shown by the bolded pads for one of the clusters in each direction.

The clustering direction depends on the angle of the track with respects to the x-axis, defined as θ . For example, a track going along the z-axis the crossing angle is defined as 90° , and a track going along the x-axis defined as 0° . In the case that the crossing angle is $45^\circ < \theta \leq 90^\circ$ the clustering direction is along the x-axis. For $0^\circ < \theta \leq 45^\circ$ it is along the z-axis.

The position along the clustering direction is calculated by weighting the individual hit's positions by their charges q_i and getting the mean value. The other direction is set to the center of the pad. For example if we are clustering along the x-axis for a cluster, the z-position is set to the center of the pad in the z-direction and vice versa.

Clustering in this way gives us better position resolution for calculating the position of each cluster. You could imagine if we calculated the clusters only along the x-axis for tracks with $\theta \approx 0^\circ$ the x-position is not well defined. By clustering in the direction most perpendicular to the track, we get a better position resolution.

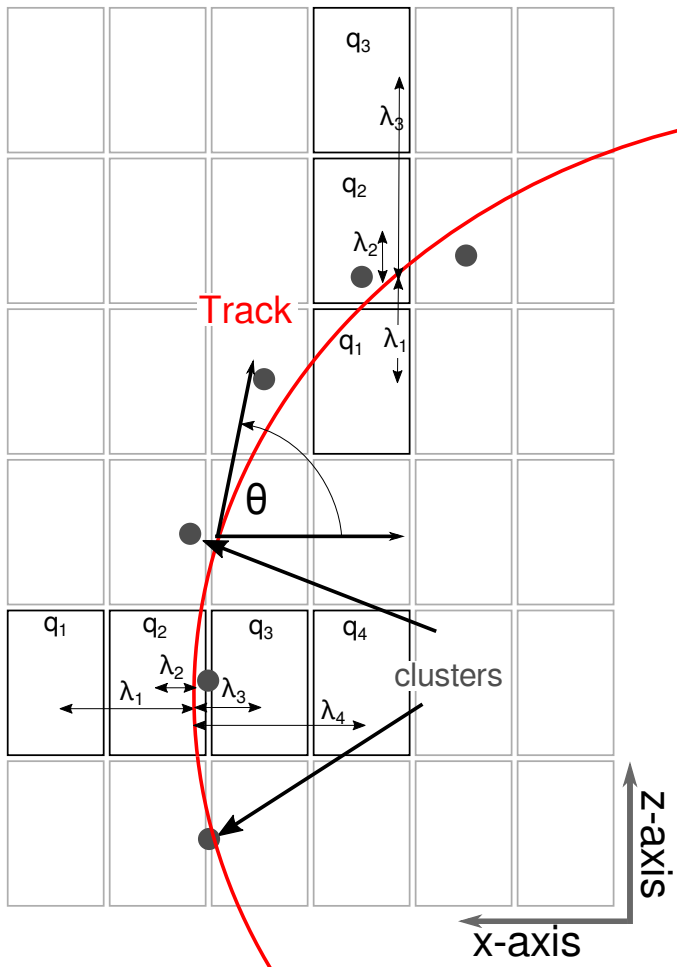


Figure 1.2: Cartoon graphic of a top down view of a fit to a track passing through several pads. The bolded pads and the charges q_i represent the hits belonging to that pad and the clusters of the track representing the average position of the track. The three clusters at the bottom are clustered in the x-direction and for the upper three clustered in the z-direction. The estimate of the position of the avalanche is given by the track fit and the position from the center to each pad to the \bar{x} position is given as λ_i .

1.1.4 Pulse Shape Algorithm

1.2 Corrections Task

1.2.1 Pad response function cut

1.3 Calibrations and Corrections

1.3.1 Gating grid noise subtraction

Opening the gating grid essentially short adjacent wires together allowing them to reach equilibrium as fast as possible. In practice the impedance of both sides was not entirely matched properly and this caused an oscillating current to bounce back and forth in an under-dampened manner. This caused residual induced signals early in the time bucket spectrum which created an extra source of noise in the data. The ground grid shielded some of the noise, but the path to ground was on two ends and was not sufficient for this frequency. Figure 1.3 shows in the upper panel the gating grid noise ADC time bucket spectrum for 2000 events in a given pad. The signal is stable within a pad and the mean value –shown as the red line– can be calculated after averaging over several thousands events. The raw gating grid noise lasts for 100 tbs extending into the real data with a decreasing amplitude.

The gating grid itself was not always stable and only the ^{132}Sn and ^{124}Sn beams were relatively stable. Several times during the ^{108}Sn and ^{112}Sn beams the gating grid broke. After several data runs were taken, we took what is called gating grid noise runs to get the profile of the gating grid noise throughout the experiment. To achieve this the anode wires would be turned off and the trigger was allowed to otherwise operate normally, firing the gating grid to open as usual. Since the anode wires were all turned off no signals would be seen except those coming from the gating grid noise. Several thousand triggers of the gating grid were taken to get a good noise profile.

Once the mean value response in each pad is calculated, we can use the gating grid noise profile runs to correct the real data and remove the noise of the gating grid. To show the best case

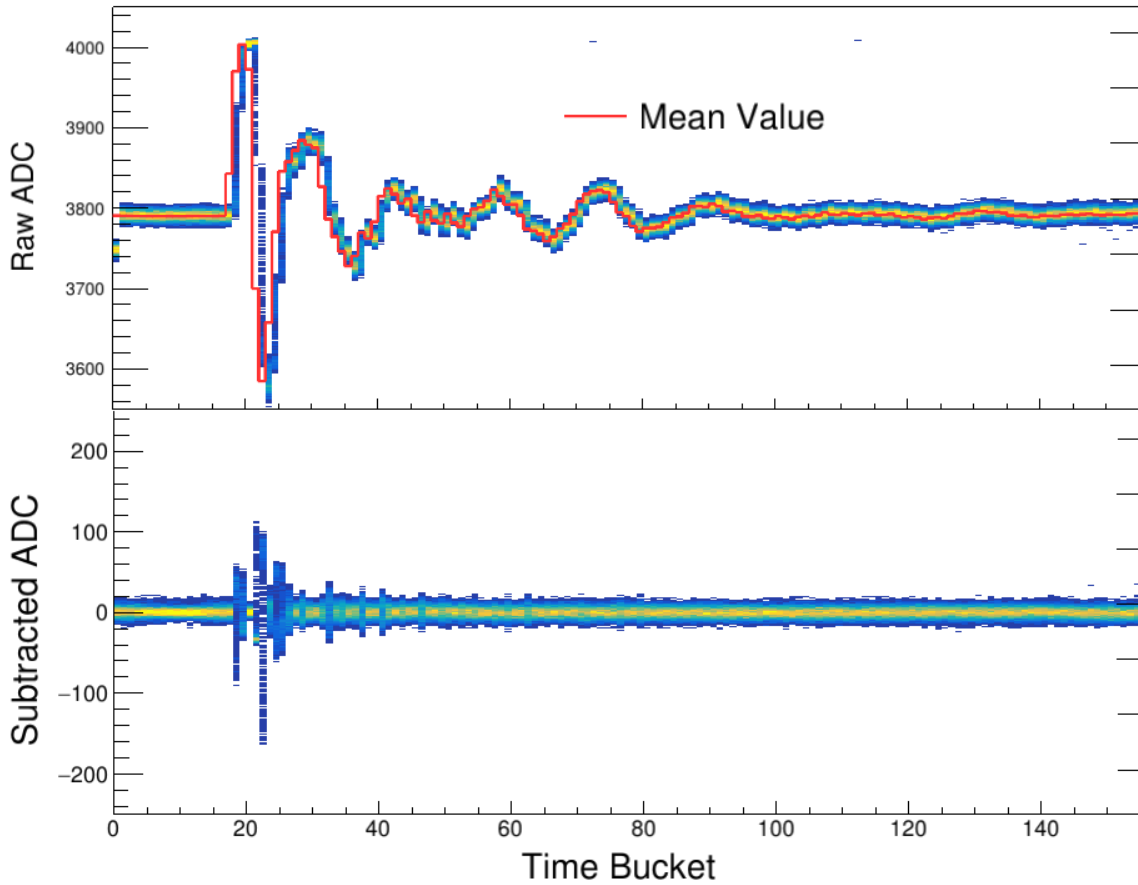


Figure 1.3: Gating grid noise profile and subtraction for a particular pad.

scenario of this technique, the bottom panel of Fig. 1.3 shows the gating grid noise self correcting itself. We can see the pedestal is already subtracted naturally when using this technique, and the subtracted ADC spectra is centered around 0. Residual gating grid noise that was not canceled by the subtraction remains but is significantly reduced to a much smaller time bucket region. This happens in regions where the gating grid noise is changing rapidly, where the ADC value is dependent upon small jitters in the timing of the signal. All time buckets below 30 tb were cut away from the spectrum to get rid of the small region where the gating grid is still opening and to remove the residual noise.

100MeV Target					
Particle	Measured	Corrected	% Difference	% Difference	
p	882.8	929.5	877.3	3.7	-1.0
d	817.1	831.15	797.94	1.7	-2.3

Table 1.1: Summary of expected cocktail.

100MeV					
Particle	Expected	Measured	Corrected	% Difference	% Difference
p	882.8	903.5	889	2.0	-1.6
d	817.1	898.5	874.5	2.1	-2.7

Table 1.2: Summary of expected cocktail.

300MeV						
Particle	Expected	Measured	Corrected	% Difference Raw	% Difference	Corrected
d	1621	1704	1612	5.1		-0.6
t	1612	1691	1596	4.9		-1.0
${}^4\text{He}$	1613	1698	5.3	1595		-1.1

Table 1.3: Summary of expected cocktail.

1.3.2 Cocktail calibration

A cocktail of several light charged particles were produced ($\text{p}, \text{d}, \text{t}, {}^3\text{He}, {}^4\text{He}$), and measured in the TPC to provide a momentum calibration of the TPC. The magnetic and slit settings of the dipoles in the BIGRIPS spectrometer was set so that the measured momentum resolution of the beam was $\delta p/p < 1\%$. Two magnetic rigidity settings were studied, with an empty target. A thick Aluminum target was used to provide a slightly lower energy point for part of the lower rigidity setting, effectively creating three calibration points over several particle species. The production of certain particles ($\text{t}, {}^3\text{He}$), produced too few counts to make a good measurement, and in the high momentum rigidity setting protons could not propagate down the line and there were no counts.

Since the expected momentum resolution resulting from the spectrometer was less than 1%, the observed momentum resolution measured by the TPC is a good representation of the combined momentum resolution of the software and TPC (intrinsic detection) system. The momentum resolution depends on several factors such as the particle's angle, momentum, charge, track multiplicity, etc. This calibration beam represents an ideal situation where the track was parallel to the pad plane and only one particle was measured at one time. The energy loss resolution can also be directly measured since each energy setting represents a monochromatic source of each particle species, which has a well defined energy loss distribution. An average momentum resolution of $dp/p = 2\%$ and the energy loss resolution of $d\langle dE/dx \rangle / \langle dE/dx \rangle = 5\%$ was measured for particles ranging from H to ${}^4\text{He}$, over the range of momenta measured in the calibration beam as summarized in Table 1.4.

Since the magnetic dipole setting of the BIGRIPS spectrometer defined the energy of each particle type, we can calculate the expected momenta of each particle species measured. Small corrections were propagated using LISE++ software which can calculate the energy loss through several materials in the beam line. These corrections resulted in a small change in the momenta. The measured momenta of the calibration beam differed significantly from the expected values as seen in Tables tables 1.1 to 1.3. This effect is attributed to inhomogeneities in the magnetic field which introduces electron drift velocity in the direction of $\vec{E} \times \vec{B}$ direction as seen from Eq.???. The $\vec{E} \times \vec{B}$ drift velocity causes the electron trajectories to shift toward the +x-axis in the TPC coordinates causing particles of positive charge (going in the -x-axis) to have a higher measured momenta than in reality. The disagreement in measured and expected momenta is upwards of 5% difference in the higher momentum calibration settings. The details of the correcting for the $\vec{E} \times \vec{B}$ effect will be discussed in the later Section 1.3.8 in a more general way which also includes correction for the space charge, which this cocktail beam does not have. The same correction technique was applied here in the special case of zero space charge, which is the special case of only having $\vec{E} \times \vec{B}$ components.

The values under the corrected column seen in Tables tables 1.1 to 1.3, represent the data

Momentum Resolution %	$\langle dE/dx \rangle$ Resolution %
1.6	4.6

Table 1.4: Summary of expected cocktail.

corrected for the $\vec{E} \times \vec{B}$ effect. A significant improvement is seen in the high momentum setting going from around 5% disagreement to within 1% agreement in the corrected data. For the lower momentum settings (Tables tables 1.1 and 1.2), protons see a slight improvement of about 1% where as the deuterons are over corrected in both settings. The level of agreement of the all corrected values is still within the estimated momentum resolution of the TPC.

1.3.3 Electronics calibration

The ADC channel number of the electronics was calibrated by measuring the response of each channel to an input pulse supplied by a pulse generator. The pulse was distributed to all the electronics channels by pulsing the ground plane for a range of input voltages. This distributed the pulse evenly across the entire pad plane. The input voltage is plotted as a function of the measured ADC channel in Fig. 1.4 for every channel. The small variation in each channel can be seen as the wide band around each measurement point. A linear fit is performed to get the best fit line which provides a reference line which each channel is calibrated to. The right panel shows the resulting distribution of channels after calibration. This is a relative calibration technique with the intent to calibrate the varying gains in each channel relative to one another.

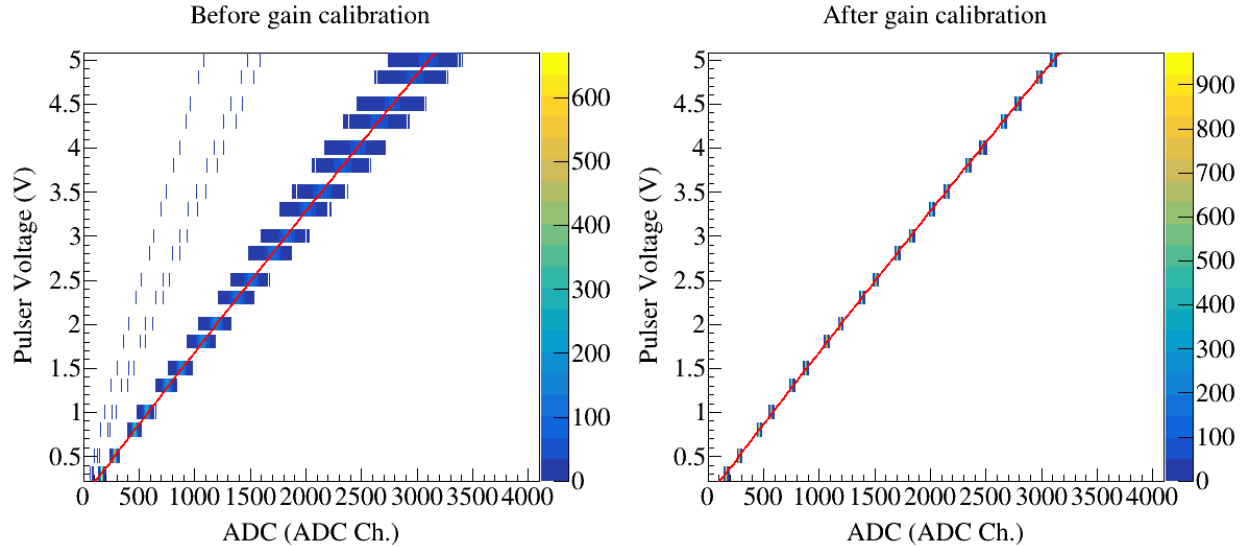


Figure 1.4: Calibration of electronics

1.3.4 Anode gain calibration

As mentioned earlier, the anode wires were separated into 14 independently biased sections. The high voltage of sections 12 and 14 were reduced during the experiment due to high currents being observed on the wires. The wire section voltages were lowered once and adjusted once again. Out of all the runs used in the analysis in this thesis .1, the anode sections 12 and 14 were lowered to 1085 V for runs 2272-2371 and set to 1214 V for all the other runs. By lowering the voltage on these anode wires, the gas gain is lowered as compared with all the other anode wire plane sections which operate at 1460 V. To account for the drop in gain, in the software we increase the gain of the pads which lie above these anode wires to match the gain in the other channels. To do so, we compare the energy loss in the high gain sections to the low gain sections to get the relative calibration factor.

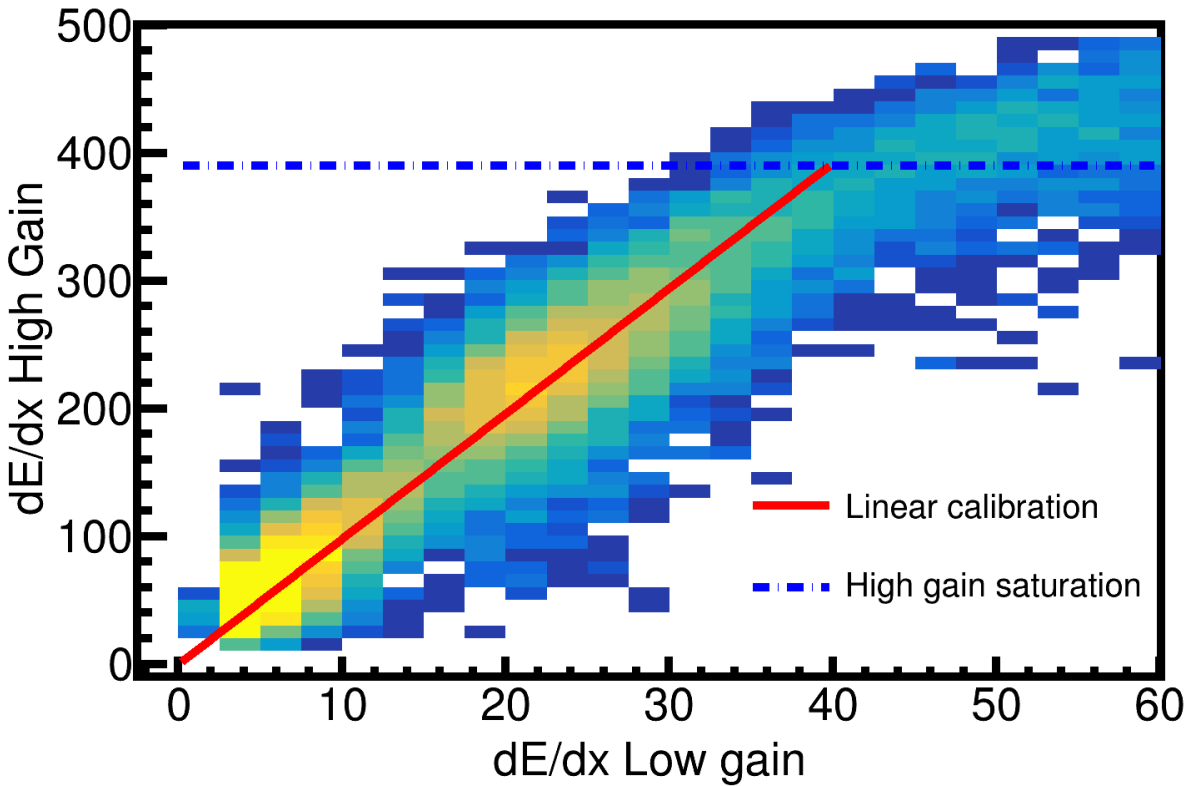


Figure 1.5: Calibration of low high.

Figure 1.5 shows the correlation plot of $\langle dE/dx \rangle$ of the high versus the low gain sections. The effects of the high gain channel saturation can around a value of 400 ADCmm^{-1} and plateaus, whereas the low gain does not. A linear fit was performed for the calibration between the high gain channel $h_c = G \cdot l_c$, where l_c is the value of the low gain channel and G is the gain factor. In the case where the low anode voltage was 1214 V, the gain factor was 9.8 whereas in the case of 1085 V, the gain factor was ??. The calibration factor was applied inside of the decoder task. A map of the channels which are impacted by the low anode wire voltages and the relevant gain was input into the software. In the decoder task the raw ADC spectra was multiplied by the input gain for a given channel. The thresholds of those channels also were multiplied by the same factor since the noise levels were also artificially magnified by the same gain factor.

1.3.5 Extending the dynamic range of the Electronics

Using a TPC for measurements of HIC in nuclear physics presents a different set of challenges as opposed to higher energy experiments. Typically in higher energy experiments the charge of particles is Ze , where $Z=1$. Also, the particles are traveling at higher energies in which the energy losses are near or close to the minimum in the energy loss curve. The dynamic range of electronics in such experiments can cover a wide range of particle energies in the energy loss curve. In nuclear HICs, we are interested in measured particles ranging from $Z=1-3$ resulting from the collision, and even higher in some applications. As seen in Eq. ??, the energy loss is proportional to Z^2 ; the energy values in nuclear HIC of intermediate beam energies (around 300 MeVA) in which the resulting particles are at much lower energies which are in the $1/\beta^2$ region. The energy range and particle types covered by the electronics are significantly limited by the dynamic range limitations of the electronics as the charge of a particle increases and the velocity decreases.

Several TPCs have tried to address this issue by having regions of low and high gain, either in amplification gain or in electronics gain. Here we run into the issue that high velocity particles will have little to no signal in the low gain regions. At lower velocities, particles will deposit much charge over the low gain regions but will saturate the high gain regions, whose charge values are usually lost. Only within the dynamic range will tracks have the best momentum resolution, outside the dynamic range clusters will be missing in the sections which depend on the track velocity, lowering the momentum resolution of tracking. There are ongoing efforts in the nuclear community to develop new electronics which hope to mitigate these persistent issues in TPC electronics CITE HERE, by being able to switch to a lower gain value when the maximum range is reached. Though, it is quite useful to develop a software technique which may extend the dynamic range of TPC electronics without the use of external hardware, especially in experiments which have already been performed with preexisting electronics technologies.

In TPCs, the effective dynamic range can be very different from the single channel dynamic range depending on the application. Typically TPCs are operated inside of a magnetic field for

reconstructing momentum of each particle, which requires sub-millimeter precision in the position determination of the track path. This is achieved by averaging the charge distribution over several pads. Therefore the effective dynamic range is related to the relative charge values of adjacent pads (between the center pad and outside pads). For example, to measure minimum ionizing particles the signal to noise ratio of the pad with the smallest charge in the distribution should be some reasonable value above noise, say at least 6:1 signal-to-noise ratio (SNR). From Section ??, we know the central pad in the cluster holds 80% of the total charge, where as the two adjacent pads each hold the remaining 10%. If we require the adjacent pads to have a SNR of 6:1, then the central pad would have a SNR of 50:1. Considering this is the SNR for minimum ionizing particles, and the maximum SNR in a channel is 800:1, this means the effective dynamic range in the TPC is roughly 16 times that of minimum ionizing particles, if we intend to have adequate position and tracking resolution.

The dashed lines and vertical blue bar in Fig. 1.6 are separated by a factor of 20, representing the typical effective dynamic range in a TPC. This dynamic range estimate should be regarded as approximate because the energy loss fluctuates significantly about the most probable energy loss, with a long “Landau” like tail, as described by Bichsel [4]. Nevertheless, the blue dashed lines and vertical blue bar illustrate that the range of energy losses sampled in a fixed gain readout system is limited. One can change the gain and shift the energy loss range that can be sampled, but the dynamic range itself cannot be increased.

The rapid increase in the stopping powers at low momentum illustrates the degree to which the effective dynamic range can be exceeded and highlights the problems encountered in studies of intermediate HICs, in which light particles with low momenta are abundantly produced along with highly charged particles. Similar problems are encountered when TPCs are used as active targets in direct reaction studies with rare isotope beams [?]. Several techniques have been employed to increase the observable range of energy losses; typically by lowering the electronics gain of selected readout channels, or by changing the gas amplification at the readout plane in certain areas of the TPC ?????. The results of changing the gas-gain, or the electronics gain, are rather similar in

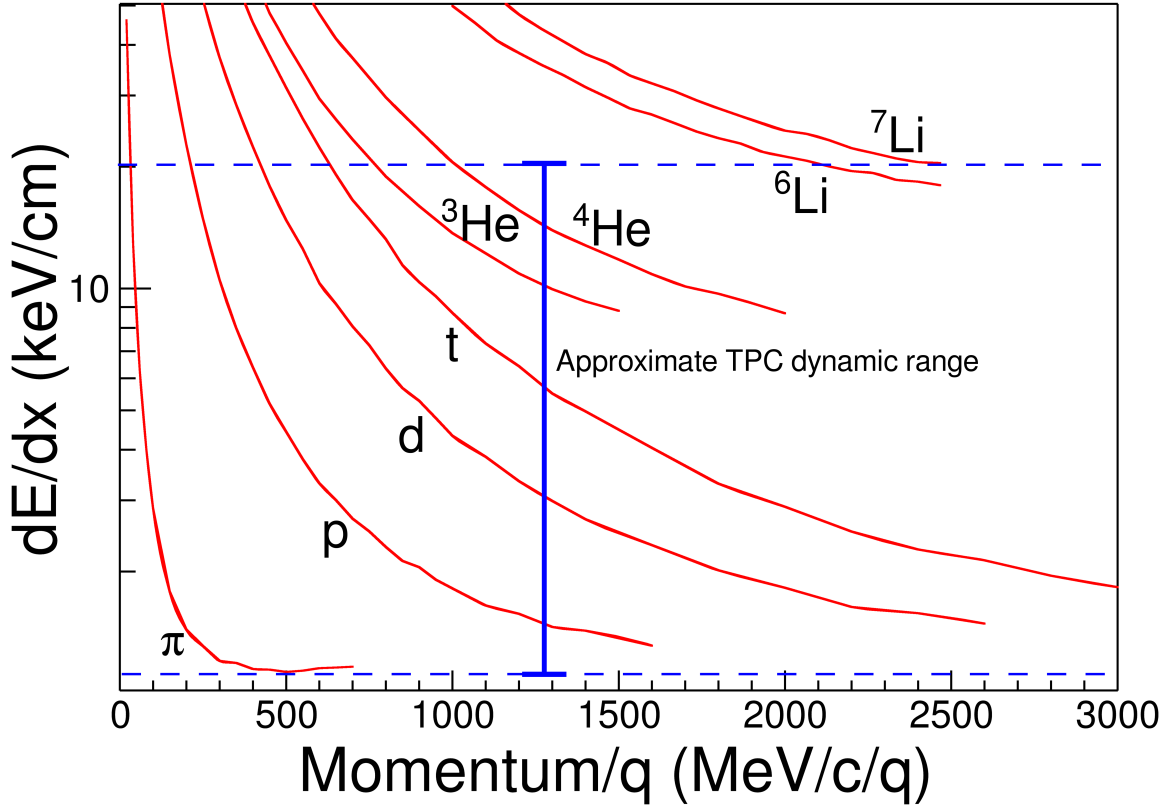


Figure 1.6: The expected dE/dx lines of different particles are given in red as calculated by Geant4. The approximate dynamic range of the TPC is shown by the vertical bar for the gain setting used in the experiment. Anything outside of this region would be saturated to some degree.

that reducing the gain to sample a range of higher energy loss makes the TPC effectively blind to minimum ionizing particles in the regions of lower gain.

1.3.6 Experimental Pad Response Function

The pad response function of the TPC was extracted from non-saturating hits and clusters in tracks at various track crossing angles. As in Fig. 1.2, we postulate that the PRF is a function of the total charge deposited in a cluster $Q = \sum_i q_i$, and the difference in position of the center of the i^{th} pad, x_i , to the mean position $\bar{x} = \sum_i x_i q_i / Q$, defined as $\lambda_i = x_i - \bar{x}$. The PRF is simply defined as the charge fraction of each pad as a function of λ , as shown in Equation 1.1.

$$PRF(\lambda_i) = \frac{q_i(\lambda_i)}{Q} \quad (1.1)$$

Averaging over many events in the experimental data, the resulting PRF for the S π RIT TPC is shown in Fig. ???. Here we see the deviations from the expected analytic Gatti distribution (black curve), whereas fitting with a two parameter Gaussian function (red curve) gives a better description of the data, Eq. 1.2, with the two parameters being the normalization coefficient, N_0 , width σ , and with a mean value assumed to be 0.

$$PRF_{\text{Gaus}}(\lambda) = N_0 e^{\frac{-\lambda^2}{2\sigma^2}} \quad (1.2)$$

The shape of the PRF depends on the crossing angle of the track [5], which determines how wide the charge is distributed along the wire. Figure 1.7 shows the PRF of π^- tracks versus the crossing angle θ of the track. The PRF gets wider starting from 90° and until where we switch clustering directions at 45° ; if we did not switch clustering directions the PRF would become wider until it was a uniform distribution and there was no position resolution. Switching from x to the z direction clustering the opposite trend is seen where the PRF becomes narrower going from 45° to 0° , as the position resolution gets better.

A Gaussian fit was performed were performed to the experimental data with 5° width bins from $0^\circ < \theta \leq 90^\circ$. Figure 1.8 shows the two parameters resulting from fitting the the Gaussian function given in Eq. ?? are plotted versus θ . A 4^{th} order polynomial fit of these parameters allowed for interpolating for any given θ value as seen by the black line.

1.3.7 Method of Desaturation

We will use the term “desaturation” to describe the process of correcting the charge values of the saturated pads. Figure 1.9 shows a typical situation of saturated signals in a given cluster of hits. When an avalanche causes a large enough induced signal, it is the pads directly underneath which collect the largest charge becoming saturated; denoted here as q_2' and q_3' . Pads further away collect less charge and typically are not saturated; the non-saturated pads are denoted here as q_1 and q_4 .

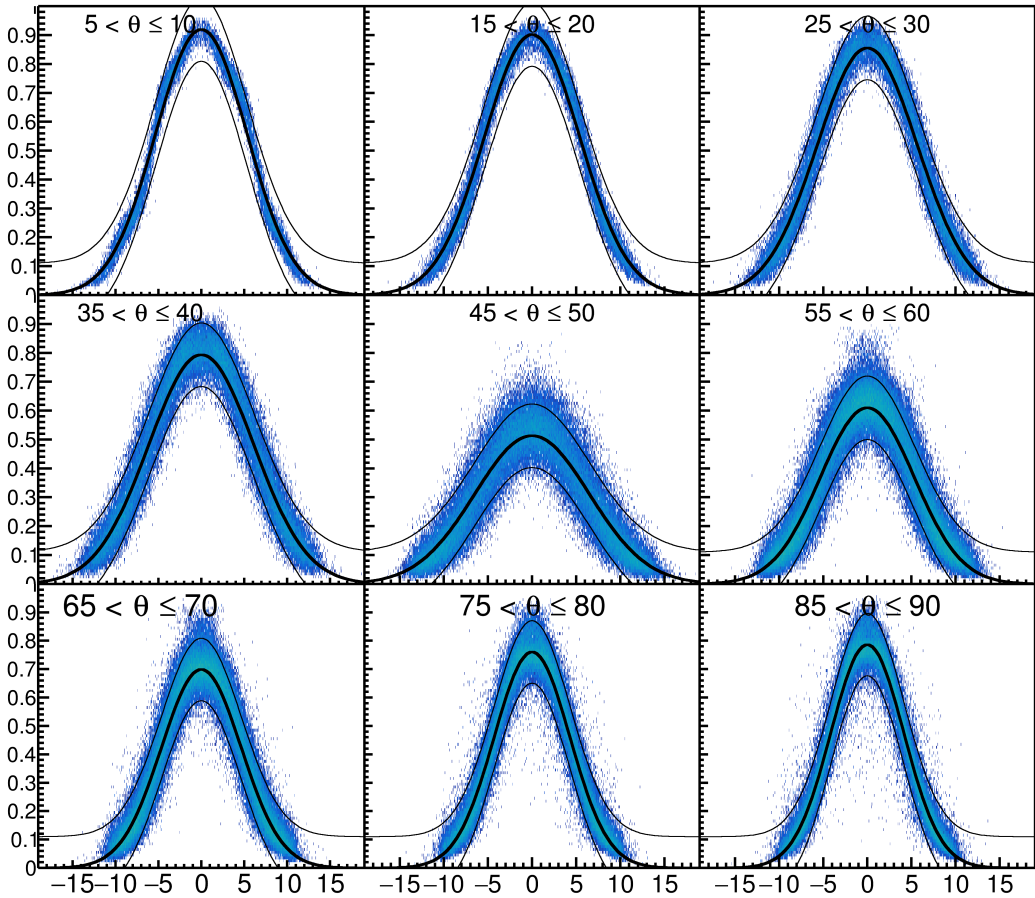


Figure 1.7: PRF response from π^- data.

Though the true charge value in the saturated channels are lost, we know that the distribution of all charges must follow the PRF which is a fixed feature of all TPCs, and has been experimentally measured above. From the tracking information, we know a given clusters crossing angle and can interpolate to get the corresponding parameters for the PRF described in Fig. 1.8.

We assume the distance of each pad to the track, λ_i , is fixed, defining the fraction of charge each pad receives as given by the $PRF(\lambda_i)$ function. To determine the best estimate for the charge values of each saturated pad, a chi squared function is minimized,

$$\chi^2 = \sum_i \frac{(q_i^{\text{obs}} - q_i^{\text{expect}})^2}{q_i^{\text{expect}}}, \quad (1.3)$$

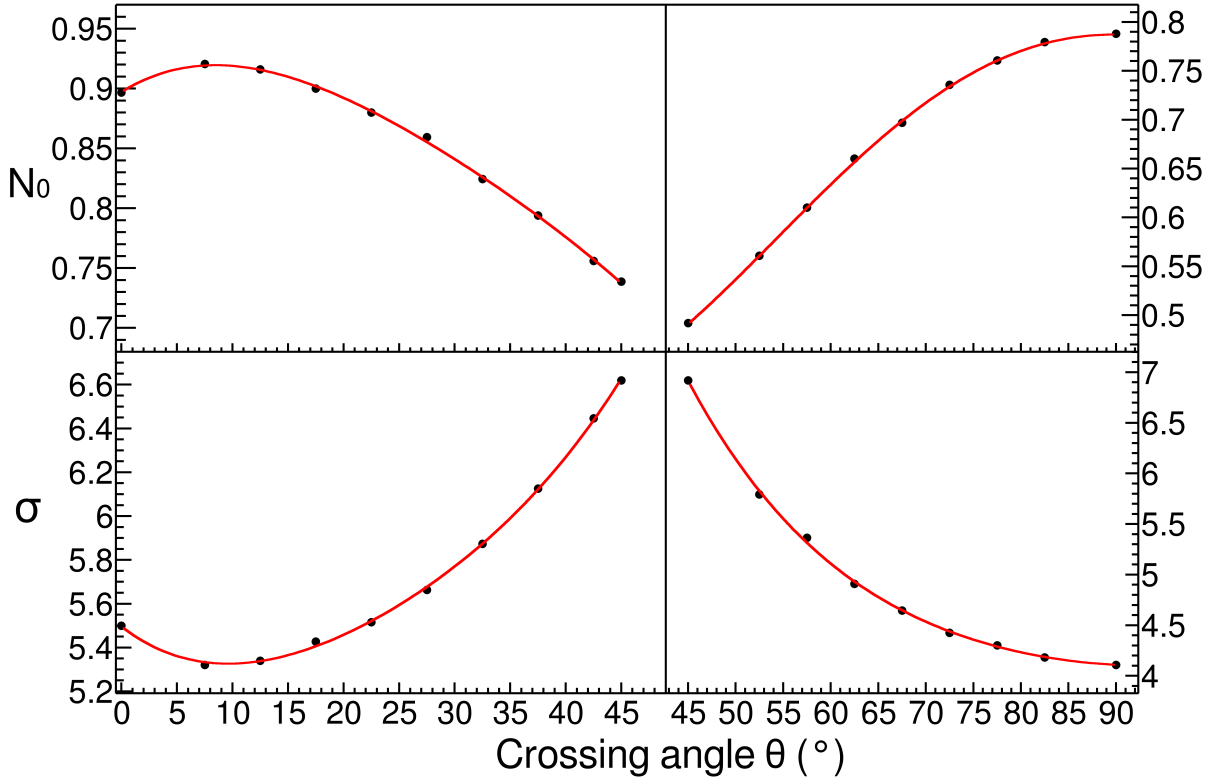


Figure 1.8: Parameters N_0 and σ as a function of the crossing angle θ with the 4^{th} order polynomial fits.

where q_i^{obs} are the non-saturated charges and q_i^{expect} are the charge values expected from the PRF calculated as $q_i^{\text{expected}} = Q \cdot \text{PRF}(\lambda_i)$. The saturated charge values q'_i are treated as unknown variables and are allowed to vary in the χ^2 minimization; the values calculated by the minimizer are added to the total expected charge Q .

Tracks which saturate pads in the high anode wire voltage region are not saturated in the low anode voltage region. By comparing the $\langle dE/dx \rangle$ values of these two sections, we can directly measure the success of the desaturation in the high gain regions. While this desaturation technique avoids the need to lower the gain of any region, the low anode voltage region proved to be a direct measurement of the success of this technique.

Figure ?? shows the the $\langle dE/dx \rangle$ values of the high gain region compared with the calibrated low gain region. The effect of saturation can be seen in the high gain region for the uncorrected

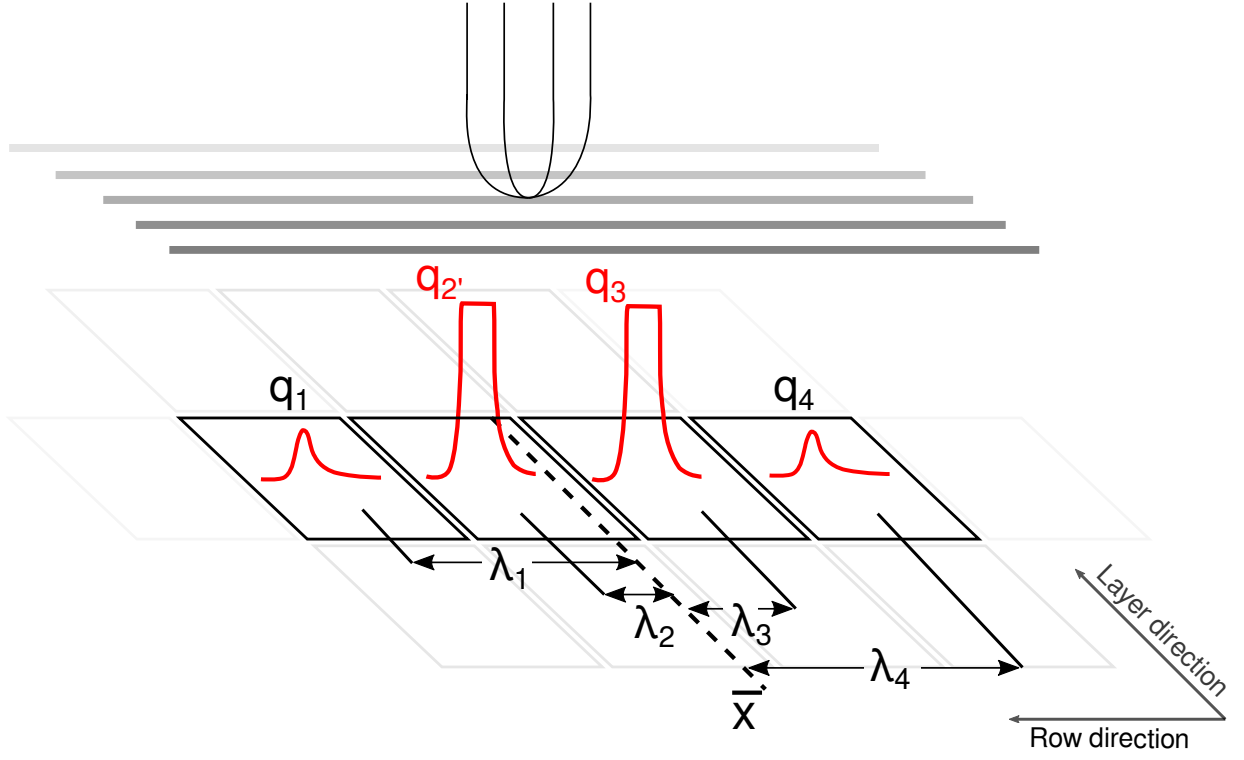


Figure 1.9: A typical case of a saturating event. The red pulses represent the time bucket signal for each collected charge. The pads directly underneath the avalanche point, q_2' and q_3' , are saturated while pads farther away, q_1 and q_4 , are not saturated.

data above values of 400 ADC/mm where the values plateau, whereas the low gain region still returns accurate values¹. Below this value the electronics are not saturated, and therefore the high and low gain sections agree.

After applying the desaturation method, the correlation between the high and low gain sections is restored, as seen in Fig. ???. From this comparison, we can approximate that the correction has corrected the high gain sections to agree with low gain sections to values of 2000 ADC/mm, increasing the dynamic range by a factor of at least 5.

The success of the desaturation becomes more clear when looking at the particle identification (PID) lines. In the following PID plots the red lines represent the most probable energy loss as given by Geant4 straggling functions. A linear calibration was performed to convert keV in Geant4 to ADC in the experiment given by $ADC/mm = 19; keV/cm$.

¹Un-calibrated ADC channels in arbitrary units.

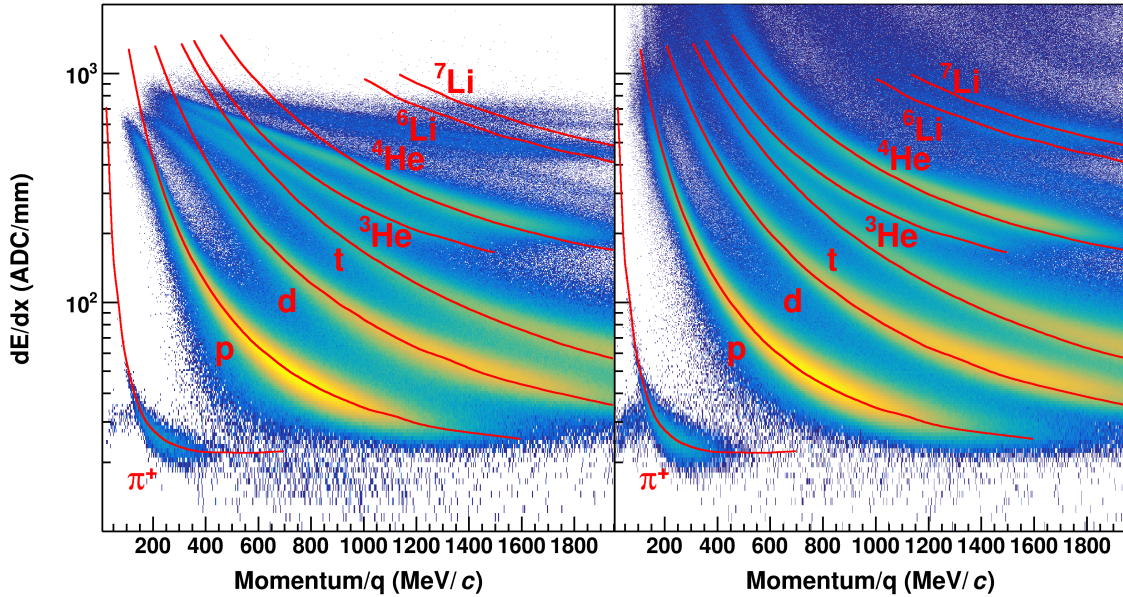


Figure 1.10: Uncorrected (left panel) and desaturated (right panel) collision data at polar angles of $\theta < 40^\circ$ and azimuthal angles between $-80^\circ < \phi < 80^\circ$

There are pronounced PID lines of several particle species in both the uncorrected and corrected cocktail beam PID shown in the subplots of Fig. ???. The uncorrected data in the left panel shows the effects of saturation; the PID lines deviate from their theoretical expectations starting at around 400 ADC/mm eventually reaching a plateau. After applying the desaturation technique – in the right panel– we see a large improvement, most notably for the He and Li particles, which suffer the most from saturation and even ${}^6\text{Li}$ and ${}^7\text{Li}$ can be separated. A more subtle improvement of the lighter particles, (p, d, t), can also be seen in the PID lines at lower momenta.

A similar effect is seen in the experimental collision data. In Figure 1.10 though the PID suffers from more background and inefficiencies than the cocktail beam we see a similar improvement in the PID lines when comparing before – the left panel– and after applying desaturation – the right panel. Notably the largest improvement is the separation of particle species at lower momenta and the separation of the Li species into ${}^6\text{Li}$ and ${}^7\text{Li}$. In these regions, there was little to no PID resolution before desaturation.

The dynamic range was extended by at least a factor of 5, as demonstrated by the improved PID lines, and quantified by direct comparison to low gain sections of the TPC.

1.3.8 Space Charge Corrections

As the beam passes through the field cage it ionizes the gas creating electron-ion pairs. The drift velocities of the ions are typically 10^4 times slower than the electron drift velocities [?, blumrol] Any source of ions have the potential to build up creating a positive space charge distorting the drifting electrons, biasing the track momentum. There are several regions of the TPC in which ion are created. The largest source of positive ions is created in the avalanche process near the anode wires. These ions slowly drift toward the cathode. If the gating grid is closed the ions will terminate there; though it opens occasionally for $11\ \mu\text{s}$ the ions only move $1\ \mu\text{m}$ in this time and will be captured by grid when it closes. For this reason, the source of ions resulting from the avalanche region is negligible.

The other source of ions come from the primary ionization produced by the beam and reaction products in the detector gas. The energy loss $\langle dE/dx \rangle \propto Z^2$, where Z is the charge of the particle type. Because the charge of the un-reacted beam is around $Z=50$, the ionization due to the beam is a factor of 2.5×10^3 times that of the light charged particles which mostly are of charge $Z=1$. It is the largest source of positive ions in the TPC.

NEED TO PUT IN ABOUT THE GATING GRID LEAK

The beam is positioned about 25cm below the anode plane in the TPC. It takes electrons approximately $5\ \mu\text{s}$ to drift to the anode plane where as it takes the ions $5 \times 10^4\ \mu\text{s}$. The beam rate in the experiment varied around a value of about 10kHz, which has an average occurrence of 1 beam every $100\ \mu\text{s}$; this is shorter than the time it takes for the ions to terminate on the cathode plane, resulting in a build up of positive ions. Figure 1.11 gives an idea of the shape of the sheet of space charge carved out by the beam path. The ions from each beam create a line charge which drifts towards the cathode with a constant velocity. The average distance between sequential ion paths is about $25\ \mu\text{m}$ apart, therefore we expect the average number of beam paths that compose the sheet charge is around 1440 tracks – where the distance to the cathode is 29.6 cm. Though the arrival time of each beam track is random, the large number of tracks and small inter beam spacing

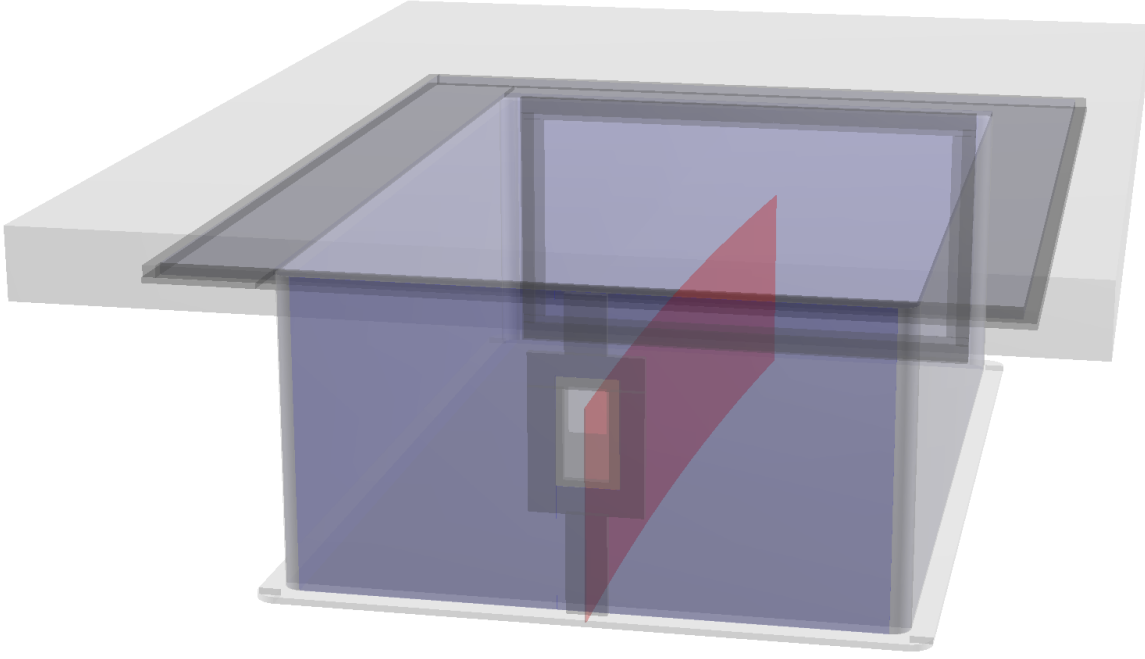


Figure 1.11: Location of space charge in ^{132}Sn

allows us to approximate the sheet charge as an uniform sheet charge.

The secondary beams entering the TPC are also composed of many species of particles distributed in a finite range around the target beam. Assuming a beam of ^{132}Sn were the energy loss in gas is 11.2 keV cm^{-1} , using the number of beams above, the conversion to electrons given in ??, and the beam path length of 135 cm , the total charge density expected is $3 \times 10^{-8} \text{ C m}^{-2}$.

The electric potential can be calculated by solving Poisson's equation,

$$\nabla^2 \phi = \rho, \quad (1.4)$$

where ϕ is the electric potential and ρ is the free charge. Since the Dirichlet boundary conditions of the field cage are defined by the cathode, walls, and pad plane, a numerical solution to the electric potential is solved through the ??? technique. The electric field is simply the gradient of the potential $\vec{E} = -\nabla \phi$.

To reduce the need to compute a new electric field for a new value of the space charge, we notice

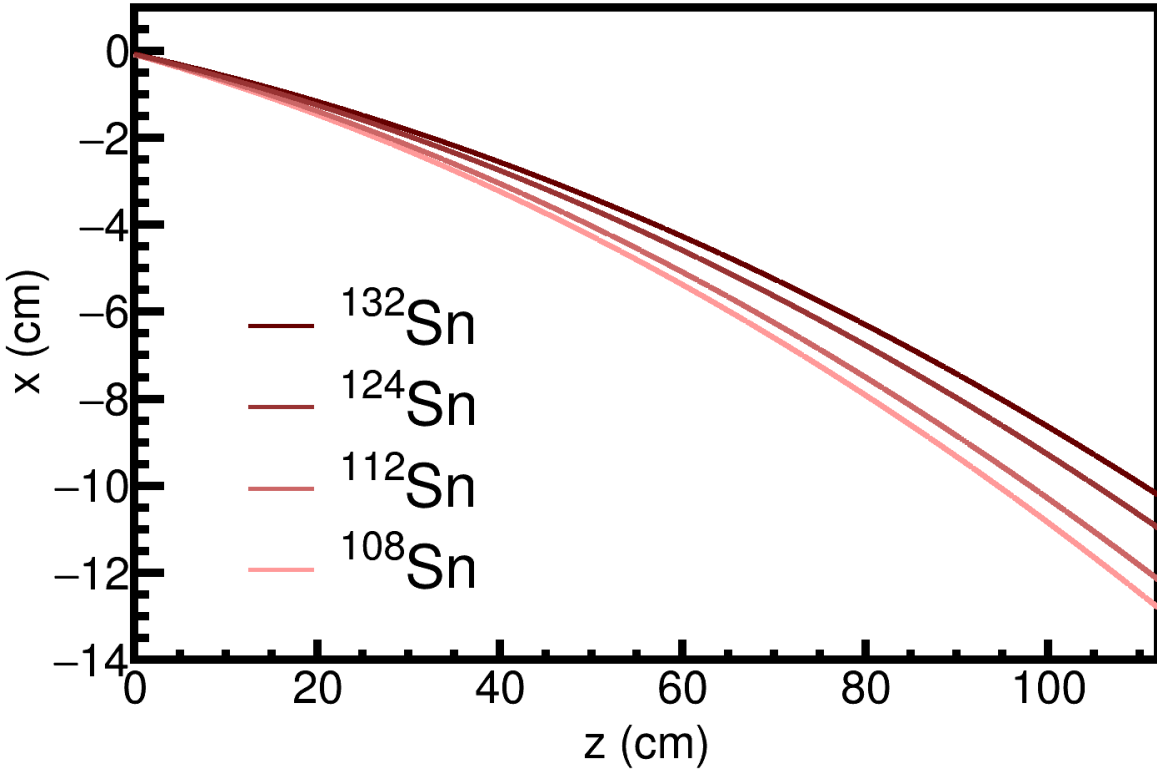


Figure 1.12: Beam path of the experiments

that $\vec{E} \propto \rho$, we can therefore solve the electric field for a certain reference charge value ρ_o , and scale the solution for any other free charge ρ by the ratio ρ/ρ_o . The full magnetic field map is provided by the SAMURAI collaboration [6]. The velocity field map can be calculated from Eq. ???. The path an electron drifts through this velocity map is propagated by using a time stepped 4th-Order Runge-Kutta integration from a given starting point of the electron. We do not add details of the electric field around the anode wires which is only relevant for the small gap between the ground and anode plane. Over this small gap the space charge corrections have very little effect.

The correction map is calculated by starting from the anode y-position and the measured position on the pad-plane (x,z), and stepping backward in time in the Runge-Kutta integration through the velocity field map until the electron reaches the measured y-position, which is split into a grid that fills the 3-dimensional volume of the field cage.

The correction is handled within the STCorrection task in the software. A data base of the sheet

charge values for every run is read in and the electric field is calculated for the reference charge for a given beam path. The electric field and velocity map is scaled by the ratio of the space charge in the particular run and the reference run ρ/ρ_0 and the correction map is calculated. The measured clusters value (x,y,z) position is input into the correction map which interpolates and outputs the correction values dx and dz which correspond to that cluster. The cluster position is shifted to new positions $x' = x + dx$ and $z' = z + dz$, before going on to the momentum and vertex finding algorithms.

It has been shown before that the amount of space charge present in the chamber is related to observables such as the distance of closest approach of each track to the vertex point [7]. In the presence of no space charge, you would correctly expect the distance of closest approach of each track to the vertex point would be a distribution centered around the true vertex location. Since the tracks are distorted by the space charge, which affects different regions of the TPC differently, a bias is introduced to the measured vertex location and widens the distribution to vertex of each track.

An example of the distortion map in the TPC is shown in Fig. 1.13 with left-going tracks shown in blue, and right-going tracks shown in green; the vectors show the direction of distortion and their magnitude have been magnified by ??? times to show the detail. The dashed lines show the effects the track shifted due to the space charge map where left and right-going tracks are affected differently. Right-going tracks tend to higher momentum values and the left-going tracks going to lower momentum values, for positively charged particles.

The inset figure of Fig. 1.13 shows the shift in the x-position distance to vertex for the displaced left-going track given by ΔV_x , with the opposite direction for right-going tracks. We will define the DOCA for left going tracks as V_x^L and for right-going tracks as V_x^R . We are able to measure the amount of distortion the space charge creates by measuring the difference between the most probable values of the left-going and right-going tracks which we define as $\Delta V_{LR} = \Delta V_x^L - \Delta V_x^R$ as seen in Figure 1.14.

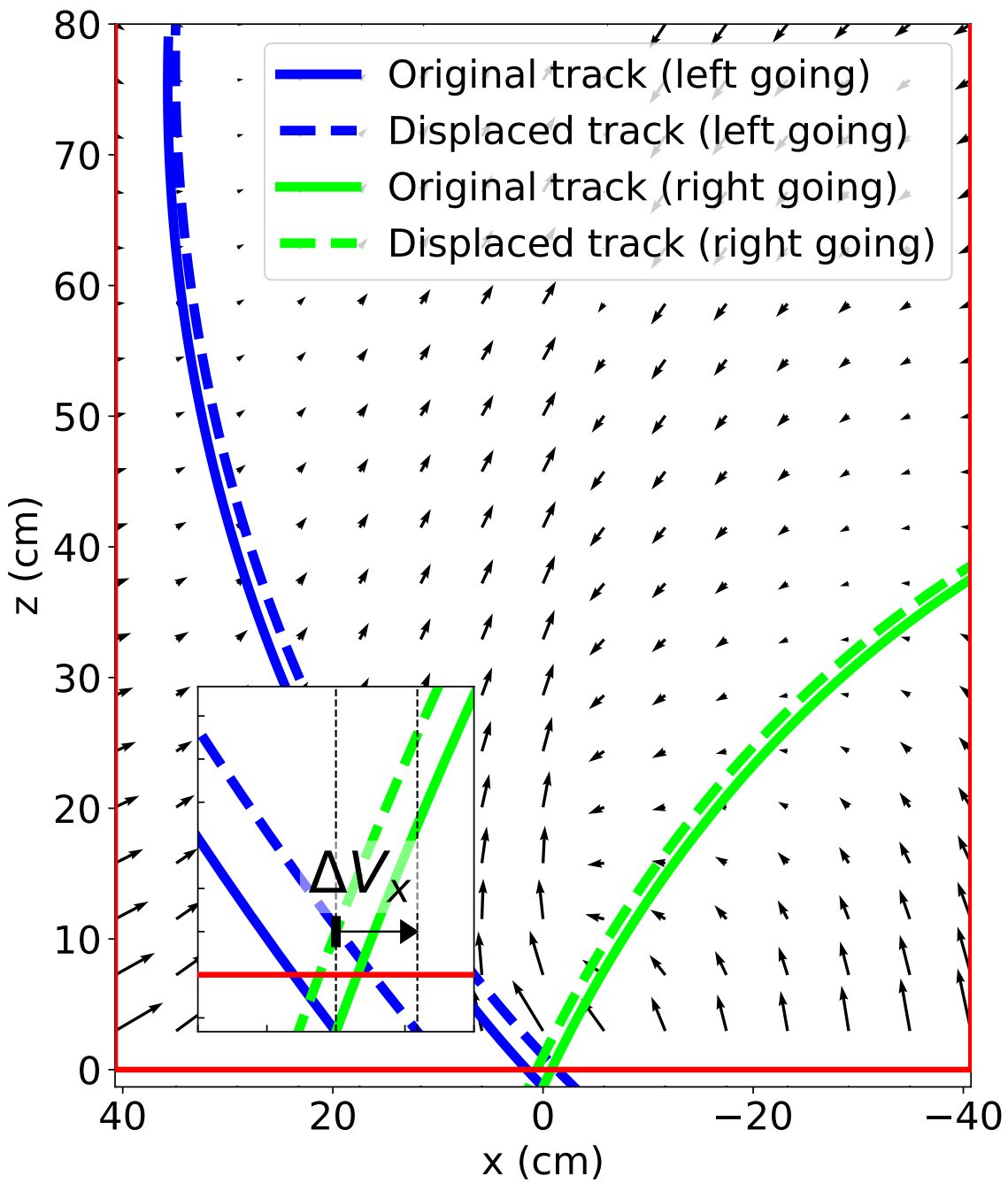


Figure 1.13: Shift of tracks

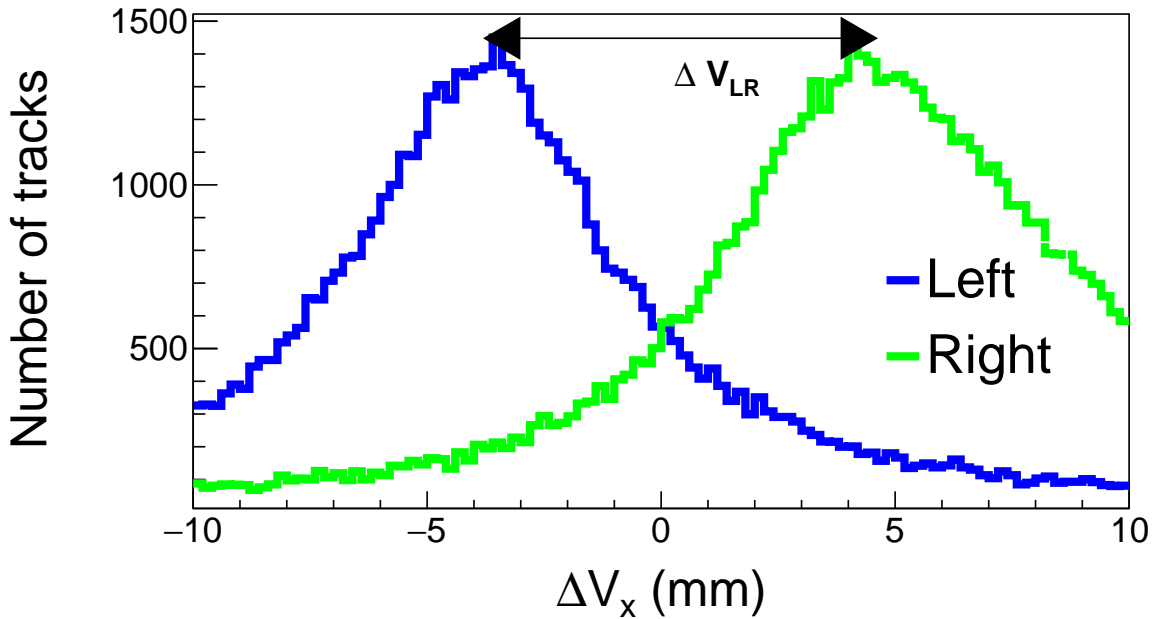


Figure 1.14: ΔV_x distribution for left-going and right-going tracks in the TPC for the

The average beam rate was recorded in each experimental run and slightly varied from run to run, due to beam production variations. The amount of space charge present in the field cage is directly proportional to the beam rate; therefore ΔV_{LR} is also proportional to the beam rate as shown in Fig. ???. The only parameter in the space charge correction algorithm is the surface charge density σ_{SC} . Varying σ_{SC} for a wide range of values the ΔV_{LR} observable is measured and plotted in the left panel of Fig. 1.17. The surface charge density which gives $\Delta V_{LR} = 0$ is taken to be the estimate for the average amount of space charge present.

This is done for several runs which vary in beam intensity though the solution for the estimated space charge value will be different. Since the surface charge density is proportional to the beam rate, a linear fit gives good agreement for interpolating the surface charge values as a function of beam rate. Figure 1.17 shows the relation of the dependence of the space charge as a function of beam rate for the ^{132}Sn system.

Following this algorithm the space charge is estimate for each run and system. Figure 1.18

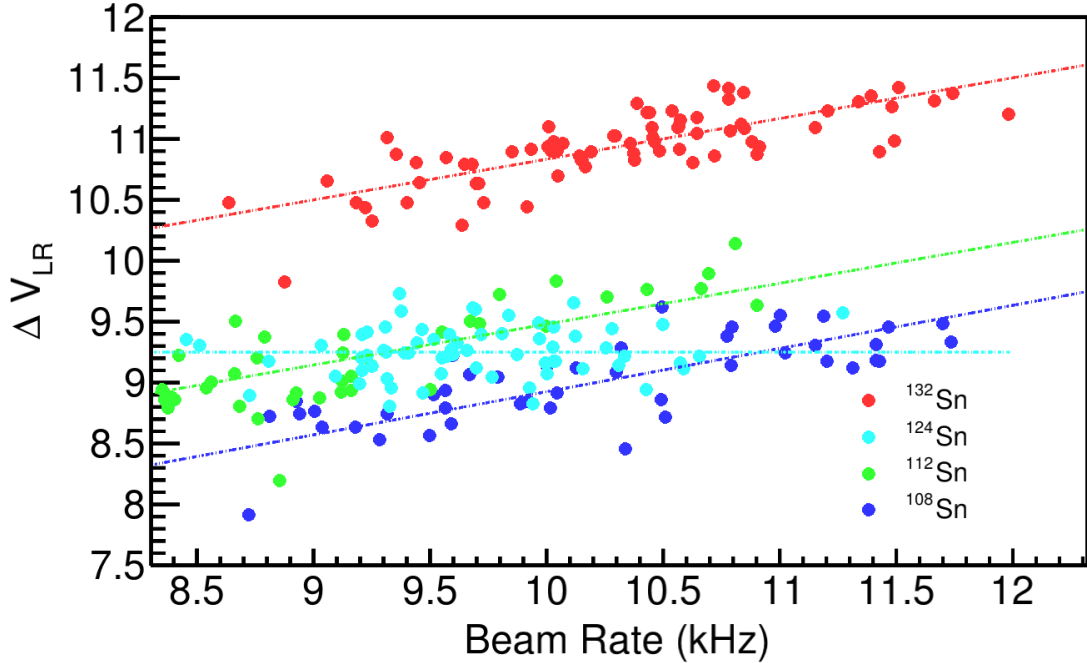


Figure 1.15: ΔV_{LR} versus the beam rate for all systems with the fitted function.

shows the summary of the extracted space charge values for each secondary beam. The linear fits relating the space charge density to the beam rate for each system is shown in Fig. 1.16 where the space charge value is inferred from the measured beam rate. Notice that in the $^{112}\text{Sn} + ^{124}\text{Sn}$ system a constant value of was assumed since the beam rate did not span a large enough range to warrant a more detailed analysis.

Adding the BDC vertex greatly improves the momentum resolution of the track fitting, but there is a systematic shift when as compared with the momentum value without using a vertex as an extra constraint. Since the space charge affects right-going and left-going tracks differently making right-going tracks differently than left-going tracks, it appears they no longer originate from the BDC which is not affected by the space charge. For tracks at polar angles of $\theta < 40$ deg, the disagreement between momentum values with and without the BDC are much less because the projection of the track does not disagree as much with the BDC point as shown in Fig. 1.20a. Figure 1.20b shows the momentum value of tracks going at polar angles of $\theta > 40$ deg are more sensitive to small changes

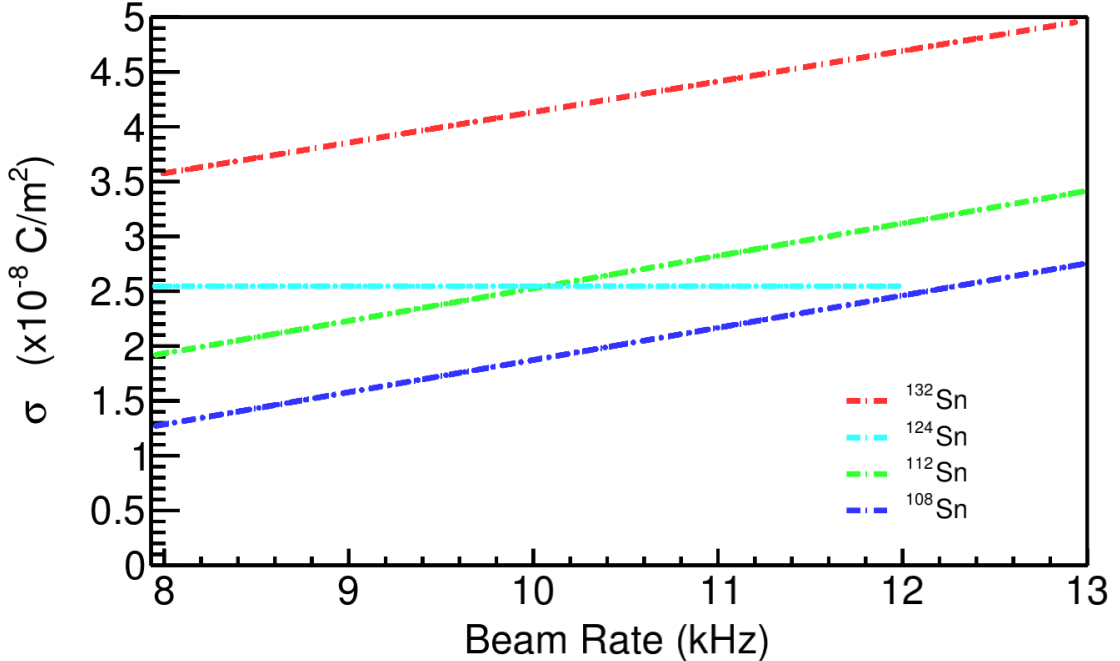


Figure 1.16: Space charge fit function versus the beam rate for all systems. These are the assumed functions we use for interpolating the space charge value from the beam rate.

in the BDC when including it as an extra constraining point. After correcting for the space charge, adding the BDC point as an extra constraint on the track does not bias the reconstructed momentum value for either $\theta < 40$ deg or $\theta > 40$ deg, which has the greatest improvement, as seen in Fig. 1.20c and Fig. 1.20d respectively. Recall that only the relative distance between left and right-going tracks was minimized; there was no guarantee that the corrected tracks coincide with the absolute BDC position at the target. This is one of the evidences of the correction's success. The others being the agreement with the expected cocktail calibration beam as described above. Later we will show how the space charge corrects the momentum distributions of left and right-going pions in the TPC.

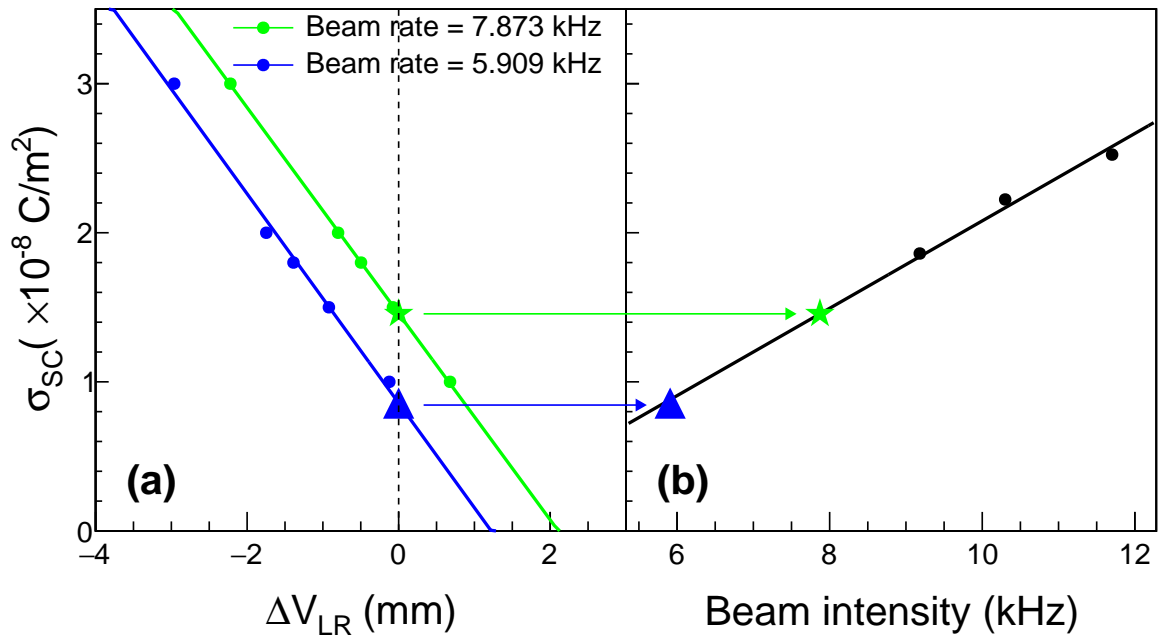


Figure 1.17: Space charge relation

1.4 Monte Carlo Simulation

The monte carlo (MC) simulation is composed of two separate simulations. The first simulation is an accurate model of the fundamental interactions of a particle passing through the various materials in the TPC; to accomplish this we have modled everything in Geant4 which also provies a particle generator. A scale model of field cage, front window, front window frame, pad plane, and aluminum top plate are modeled with the correct material type and dimensions assuming P-10 gas at a density of 1 atm. The magnetic field map of the SAMURAI dipole magnet was imported into Geant4 as well after assuming rotational symmetry along the axis perpendicular to the pole face. Along with the energy loss and particle transport, Geant4 also handles multiple scattering, and particle decay. The output of the particle generator is a series of energy loss points which contain the amount of energy lost in keV cm^{-1} and the location of the energy loss in Cartesian space (x, y, z).

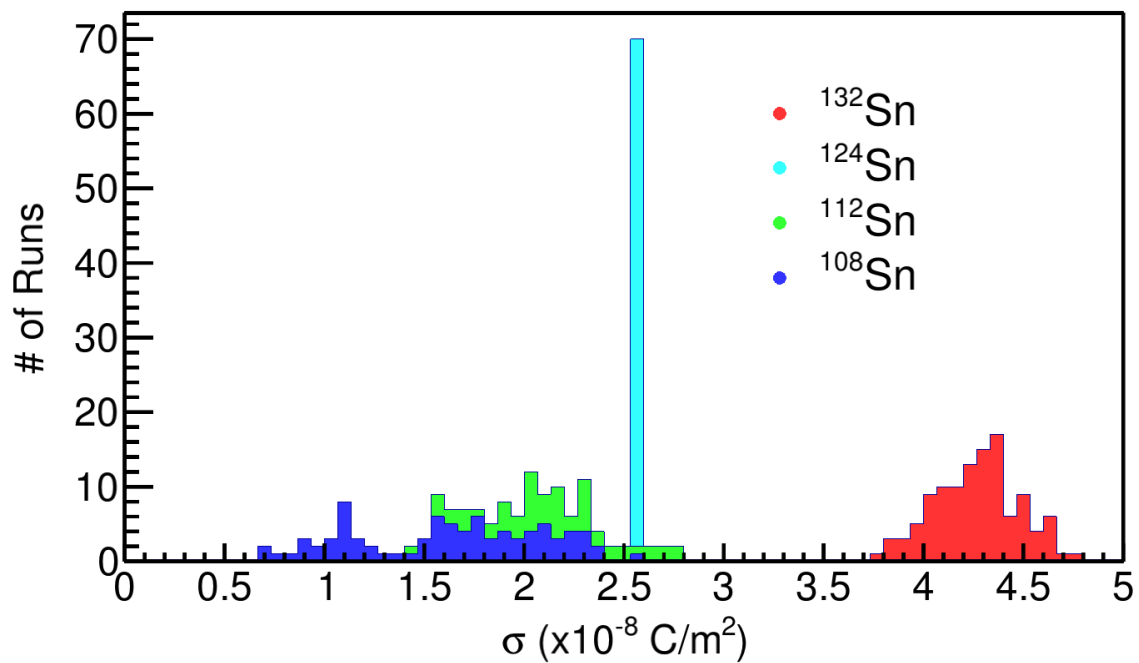


Figure 1.18: Distribution of estimated space charge densities for each beam type.

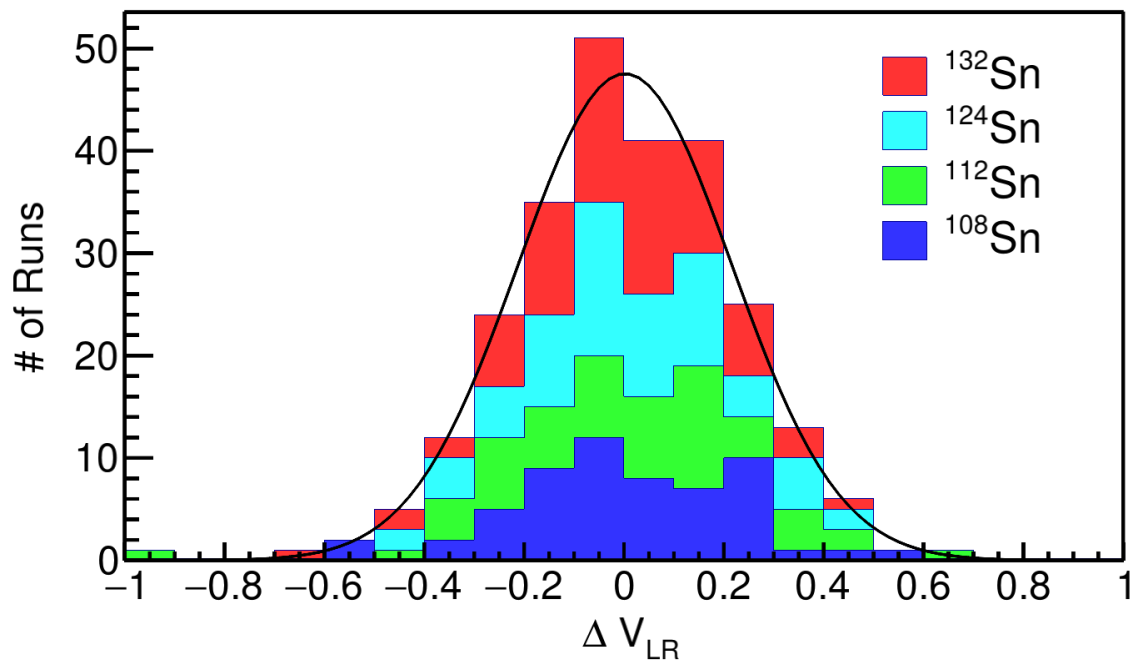
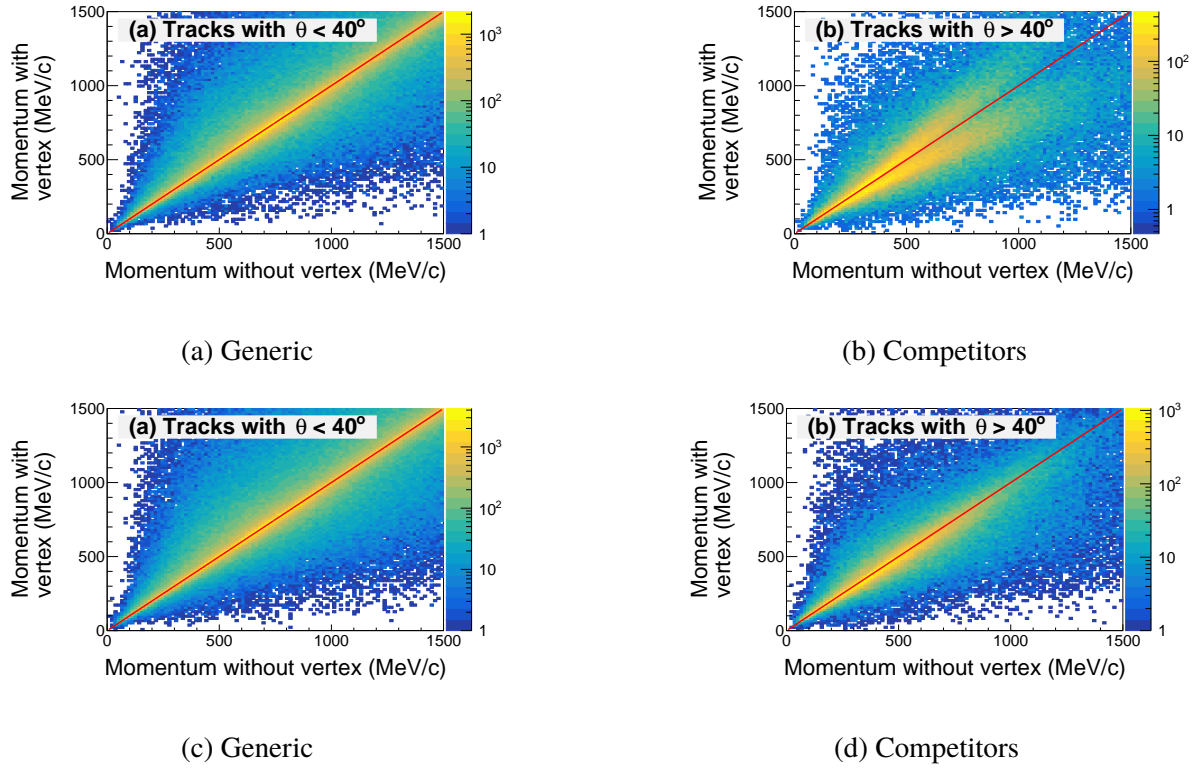


Figure 1.19: Residuals in the fitted line of ΔV_{LR} observable for all systems.



In the second part of the MC simulation, the physical processes involved in the operation and measurement of the TPC are simulated, such as the electron drift, avalanche process, and all processes involved in the signal creation in the electronics, simulating the detector's response to a MC track. This is separated into three software tasks, the drift, pad response, and electronics tasks. In the following section we will discuss these tasks in more detail, the discussion of Geant4 is not covered here and is left to the reader to explore.

1.4.1 Drift Task

The first step of the drift task is to convert the primary ionization points of the MC track provided by Geant4 into electrons. The average number of electrons created in a gas, N_{e^-} , can be described as,

$$N_{e^-} = \frac{\Delta E}{I}, \quad (1.5)$$

where I is the ionization coefficient of P10 gas (Table 1.5) and ΔE is the energy loss deposited

Electron Transport Gas Properties	
Drift velocity	5.53 cm μs^{-1}
Transverse diffusion	240 $\mu\text{m cm}^{-1/2}$
Longitudinal diffusion	340 $\mu\text{m cm}^{-1/2}$
Gas Ionization	26.2 eV

Table 1.5: An overview of the properties of the TPC

in units of eV. Since the electric field set up by the field cage is uniform for the most of the area covered by the pad plane, we assume a straight line trajectory for each electron until it reaches an anode wire. The total length drifted from the initial primary ionization point to the final anode wire is given by L_{anode} .

Drifting electrons frequently collide with the detector gas causing them to change direction. This stochastic motion is described by a diffusion process occurring along the direction of travel (longitudinal) and transverse to the motion. The longitudinal (c_l) and transverse (c_t) diffusion coefficients are determined by Garfield++ calculation in the presence of a 0.5 T magnetic field, listed in Tb. 1.5. The diffusion process is modeled by randomly sampling from a Gaussian distributions describing both of the directions. The random shift is then added to the final position of the electron. The deviation in the transverse direction, dr , is randomly sampled from,

$$dr = e^{-\frac{r^2}{2\sigma_t^2}}, \quad (1.6)$$

where $\sigma_t = c_t \cdot \sqrt{L_{anode}}$. The Cartesian directions are given by $dx = dr \cdot \cos(\alpha)$ and $dz = dr \cdot \sin(\alpha)$, where α is a random angle from 0 to 2π , since there is no preferential angle of emission in the transverse plane. The shift associated with the longitudinal diffusion, dl , is randomly sampled from,

$$dl = e^{-\frac{t^2}{2\sigma_l^2}}, \quad (1.7)$$

where $\sigma_l = c_l \cdot \sqrt{L_{anode}}$.

The final position of the electron along the wire is calculated $x' = x + dx$. Since the electron will terminate on the closest anode wire the anode wire that is closest to the shifted z-position $z' = z + dz$, the final electron z position is then updated to the anode wire it terminated on. The total drift time of the electron t is calculated as,

$$t = \frac{L_{anode} + dl}{v_d} + t_{offset}, \quad (1.8)$$

where v_d is the drift velocity. The parameter t_{offset} aligns the MC time bucket spectrum with the data. This is because the y-position corresponding to time zero in the data time bucket spectra does not correspond to the same position in the MC for time zero. This value was found to be 23 ns by aligning the MC vertex to the data vertex.

The total number of electrons produced in the avalanche process of a single electron was simulated in Garfield++ as seen in Fig. 1.4 for the anode wire voltages used in the experiment. The number of electrons produced in the avalanche is randomly sampled from the corresponding distribution depending on which anode wire section the electron terminated; the number of electrons produced is stored as a number instead of multiple instances of the original electron to save space and computation time. We assume that the lateral movement along the wire arising from $\vec{E} \times \vec{B}$ effect near the wire is negligible as compared with diffusion and other effects described later.

It is worth mentioning there is the possibility to simulate the space charge effects in this class where the inverse to the correction map described in 1.3.8 is applied to the drifting electrons. This is not used for calculating the response of the TPC for efficiency calculations since it is a trivial exercise to input the space charge map and correct for it using the same inverse map.

1.4.2 Pad Response Task

The total charge of each avalanche must be distributed according to the pad response function (PRF) described in section ???. The PRF is simulated as the double integral of a 2-dimensional Gaussian. The final output charge on all the pads are the superposition of the PRFs of all drifted electrons.

The MC PRF is expressed as,

$$PRF(x, z) = \iint e^{-\frac{(x-x_0)^2}{2\sigma_x^2}} e^{-\frac{(z-z_0)^2}{2\sigma_z^2}} dx dz, \quad (1.9)$$

where $\sigma_x = 3.4$ and $\sigma_z = 3.5$, and x_0 and z_0 are the final position of the drifted electron. The σ parameters were determined through an iterative comparison matching the PRFs of the MC and experimental data sets.

1.4.3 Electronics Task

The purpose of the electronics task is to simulates the electronics response to the charge induced on each pad, converting charge into ADC channels. The induced current in the pad goes through a pre-amplifier and shaping amplifier which determine the final pulse shape that is read out. The pulse shape did not change significantly in any circumstance, such as pulse height, data type, or particle type, as long as the electronics settings are fixed. This allows us to assume the pulse shape is constant and can be described by two variables, the height of the pulse, Q , and the starting time bucket of the pulse, t_0 . The starting time of the pulse is defined as the time at 10% of the rising edge. The shape of the pulse depends on the shaping time constant which was set to 117 ns for the data analyzed here. Figure 1.21 shows the pulse shape which was extracted from the experimental signals in the data. These were signals that did not saturate the electronics and was averaged over a wide range of ADC values. Here it is normalized so the maximum height is 1.

Converting the charge in each pad into the height of the ADC response in the electronics is calculated as,

$$Q = f_G A_{tot} \cdot e \cdot \frac{ADC_{max} - ADC_{pedestal}}{f_c} \quad (1.10)$$

,

where e is the charge of an electron in fC, A_{tot} is the total number of avalanche electrons, $ADC_{pedestal}$ is the pedestal (300 ADC, ADC_{Max} is the maximum allowed ADC value (4096),

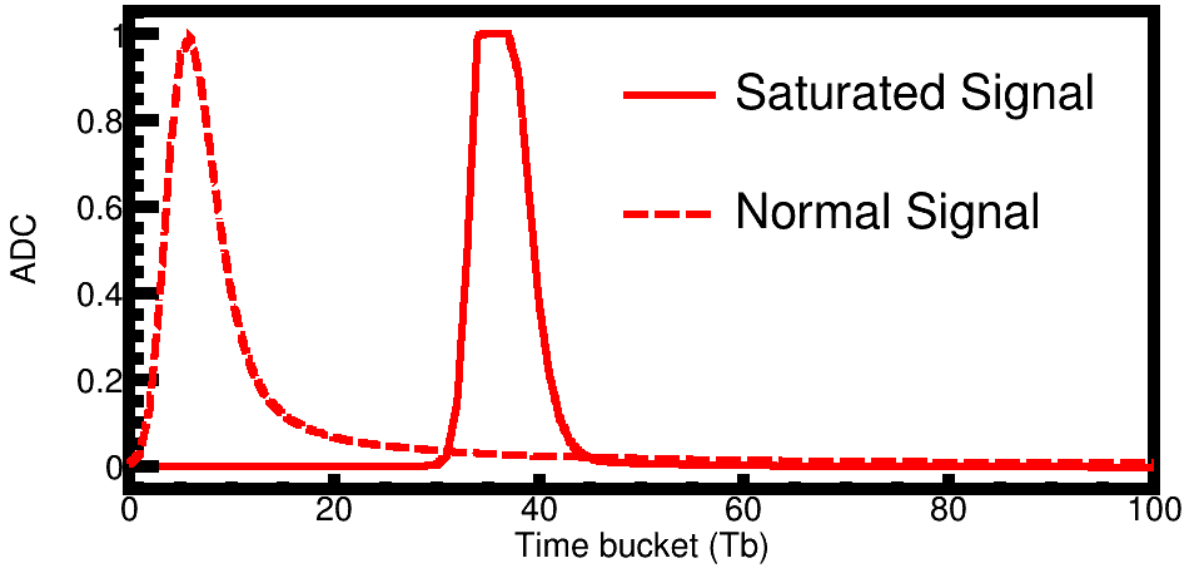


Figure 1.21: Standard pulse

and f_c is the dynamic range setting (120 fC). The pulse shape given in Fig. 1.21 is multiplied by the pulse height Q giving the full time bucket estimate of the TPC response. Random Gaussian noise is added to each time bucket where the root-mean-squared value of the electronics noise was measured to be around 6 ADC. The timing information of the pulse is calculated from Eq. 1.8. The coefficient f_G corresponds to a factor which allows for fine tuning of the ADC calibration. This factor is calculated by

$$f_G^p = \frac{\langle dE/dx \rangle_{Data}^p}{\langle dE/dx \rangle_{MC}^p} \quad (1.11)$$

where $\langle dE/dx \rangle_{MC}^p$ and $\langle dE/dx \rangle_{Data}^p$ are the energy loss values for a particle in a given momentum bin p . The calibration will be discussed later in more detail.

1.4.4 Simulating Saturation

There are several types of saturation that must be simulated or accounted for to correctly model the TPC response. They all are varying degrees of the same effect which manifest in different ways in the detector. In general all amplifiers have a finite range of output values set by a positive and

negative rail (typically -12V and +12V). If the input charge into a charge sensitive pre-amplifier causes the output voltage to reach the max (or min) output voltage, the electronics is considered saturated and the response may be non-linear. The picture is complicated by the fact that there is usually an RC feedback loop which dissipates the input charge. The time a pre-amplifier returns to linear behavior depends on the input charge and how quickly it can be dissipated [8]. The pad is otherwise considered dead and no further charge can be measured until the channel can recover.

Due to the long, high energy tail in the energy loss distribution of a particle traversing matter, it is common to see pads along the track which have collected large energy loss values saturating the electronics of that pad. This occurs for all tracks, even for minimum ionizing tracks; saturation in this case is infrequent and not an issue as there are many other clusters are not saturated. Yet as the charge of the particle gets higher, or the momentum gets lower, the most probable energy loss value also becomes higher, and a significant fraction of pads in a track may be saturated. In Section 1.3.7, we outlined an algorithm to correct for the saturation for a track, where as here we are interested in the effects saturation has on surrounding tracks to properly simulate the effect in the MC simulation.

Pads that saturate have no signal or "dead" for a given amount of time which depends on the amount of input charge. For charges that are relatively at or above the level of saturation, the pad will certainly be dead for the remainder of time after the saturating event. Signals that would have arrived later in time from other tracks passing underneath the saturating track will therefore not be measured; the saturated pad is "shaddowing" any future signals. As the track multiplicity of an event increases, the probability earlier tracks shaddow later tracks increases. This will change event by event and is very difficult to simulate except through a MC track embedding approach which will be discussed later.

In the case where the input signal is very large, the electronics can be dead for up to 35 ms [8]. The beam rate in the experiment was about 10 kHz, which corresponds to an average of 100 μ s between subsequent beams. In this case channels can be effectively dead for several events before recovering. Due to the large charge of the beam, a large amount of very high energy electrons –delta

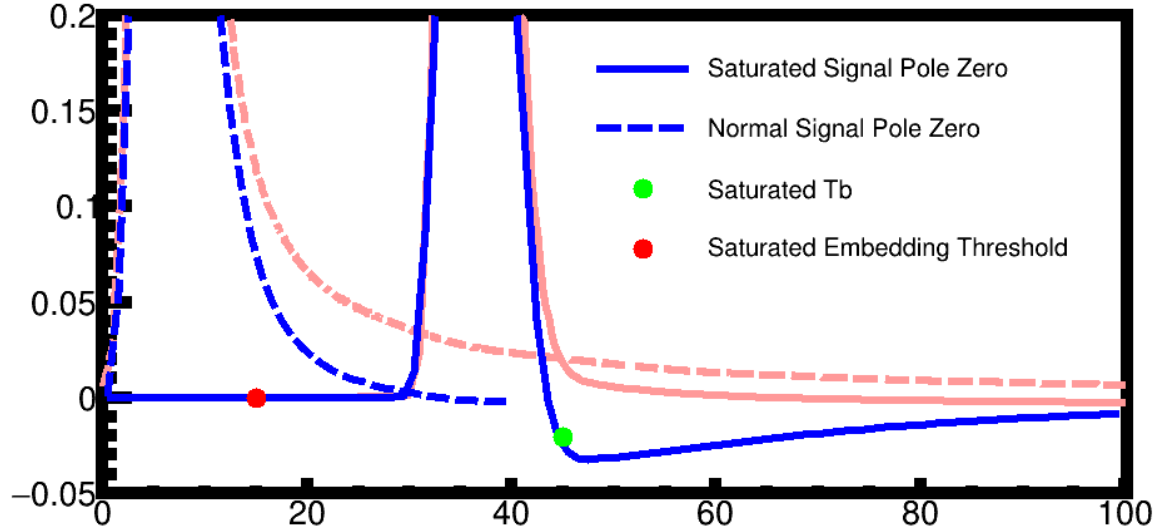


Figure 1.22: Pole zero correction

rays— are produced from the beam passing through the gas. In the presence of the magnetic field the radius of curvature of most of the electrons are within several cm in the xz-plane. Figure 1.23 shows the horizontal extent of the delta rays in a top down view of the TPC. While some of the electrons can stop in the gas, some electrons have a high enough kinetic energy going in the vertical direction, penetrating the gating grid without being blocked. They then either terminate on the pad or possibly deposit their charge directly in the pad. The charge induced on the pad is large enough to kill the pad for a time long enough to last until at least the next event. This type of saturation is randomly distributed for pads sitting directly in the beam path and are dead for that event and the next event.

The simulation of these saturation effects is handled naturally by embedding MC tracks into real data. Once the time bucket of the saturating signal has been identified, no further signals are embedded since the pad is assumed to be dead. In the case a pad is dead for the whole event, the time of saturation is set to the first time bucket and no signal is embedded at all.

The characteristic signature of a saturated signal is the fast fall time of a pulse, which quickly reaches zero, as opposed to the long tail of normal pulses as seen in Fig. 1.21. The long exponential tail can be effectively removed by a simple software technique which is similar to the electronics

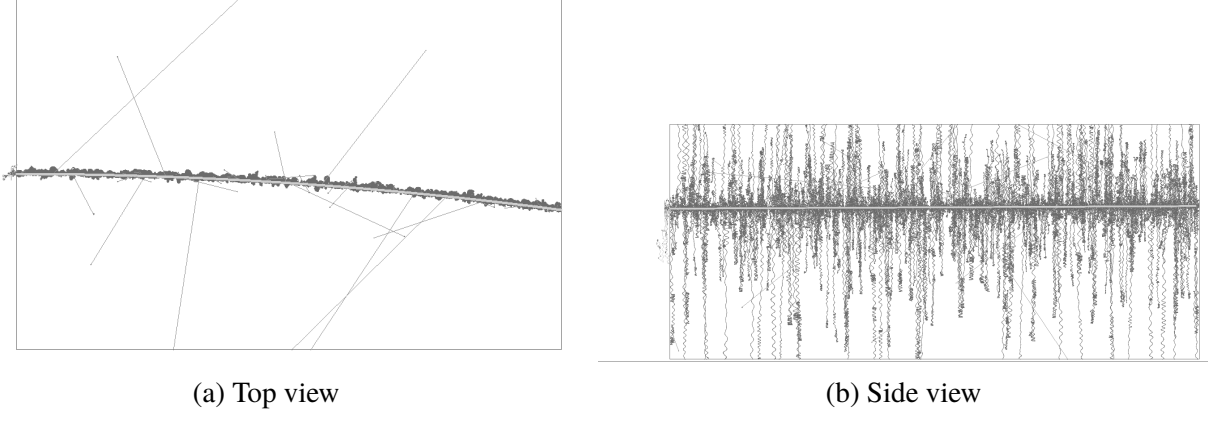


Figure 1.23: Geant4 simulation of ^{108}Sn beam at 270 MeV/A in P10 gas. Notice the extent of the delta electrons in the vertical direction as compared to the horizontal extent.

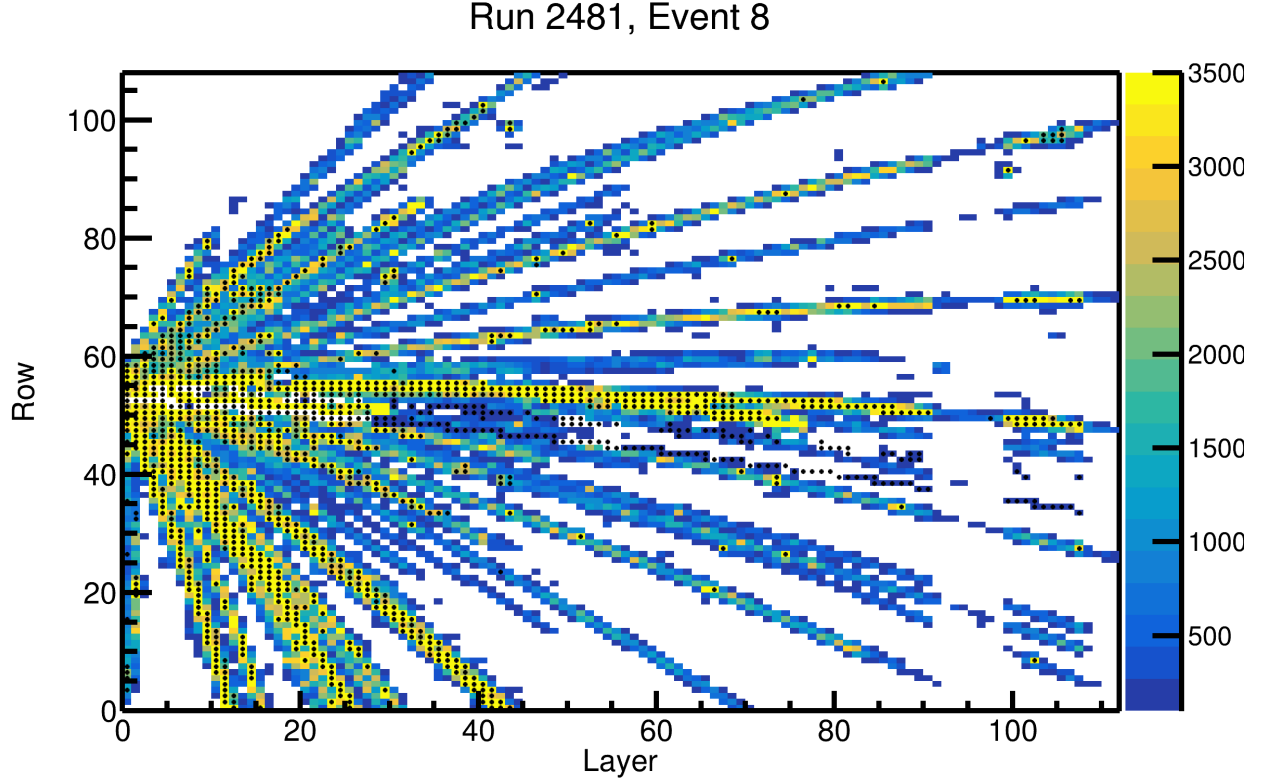


Figure 1.24: Tagging the saturated pads.

concept of “pole-zero compensation”. If the raw ADC value at a particular time, i , is represented as f_i , the corrected pulse which differentiates out the exponential tail, f'_i can be expressed as,

$$f'_i = \frac{-b_1 \cdot f'_{i-1} + a_o \cdot f_i + a_1 \cdot f_{i-1}}{b_o} \quad (1.12)$$

where $a_o = .9723$, $a_1 = -.9453$, $b_o = .9545$, and $b_1 = -.9203$. These coefficients correspond to the case where the long tail of the standard non-saturating goes to zero, without producing any negative undershoots. In the case of applying this technique to the saturated pulse, the correction produces a negative undershoot since there was no long exponential tail to begin with. Figure 1.21 shows the pulses as the red curves, and after the pole-zero compensation as the blue curves for both the normal and saturated pulses.

By applying this technique to the real data we can identify whether a pad has a saturating pulse in it and what is the time bucket location by looking for this negative undershoot. A negative peak is identified as a saturated signal if it exceeds the threshold of less than $-20 \cdot G$ for more than 8 time buckets and the max ADC value is $> G \cdot 500$ where G is the gain calibration of the pad. The max ADC condition eliminates false positives which come from dead pads where the gating grid subtraction is still applied introducing false negative peaks. The pad is then flagged as saturated and the data time bucket position of saturation is set to $t_{peak} - 5$, where t_{peak} is the time bucket of the negative peak, since the falling edge is around 5 time buckets after the beginning of the saturation. A separate time is also stored called the MC time bucket position which sets the point in time in which a signal cannot be embedded any further. This time is set to $t_{peak} - 30$ to ensure that the MC embedded signals do not overlap the real saturating data signal, which would be impossible.

Saturation can also occur if of all the pulse heights within the time bucket spectrum add to a value over the max ADC threshold of 3500 ADC. This arises because the fall time of the pre-amplifier circuit is much longer than the time bucket measurement window and pulses are allowed to pile up in the pre-amplifier. In this case no single pulse will reach over the max ADC value yet the last pulse to create saturation will have a pulse shape that has no long tail but otherwise look like a normal pulse. These pulses are also identified by the algorithm described above since there is still no long tail. When embedding tracks into pads, we do not consider the previous amount of total charge in the pad. We assume this method of saturation is a higher order correction and

the current algorithm approximates most of the saturation effects which progress through the first process. Figure 1.24 shows all of the pads tagged by the algorithm as saturated for an event in the TPC. The max ADC values in a given pad are colored and the black dots represent saturated pads. Some pads appear to be below 3500 ADC, but upon further inspection they satisfy the second process of saturation where the sum is greater than the max ADC value.

Dead pads are identified earlier in the software in the STCore class. A dead pad is simply a pad which only contains electronic noise and no signals. A dead pad is identified by having a total ADC r.m.s. value of less than 50 ADC and a max ADC < 50 over the full time bucket spectrum. Here the dead pad is also tagged as saturated and the time bucket position of saturation is set to the first time bucket.

NEED TO ADDRESS WHY THE MAX ADC THRESHOLD IS 3500

1.5 Monte Carlo Track Embedding

Track embedding is the process of taking a MC simulated track and embedding its response into an experimental data event. After reconstructing this new embedded event we match the input MC track to the corresponding final reconstructed track. By doing so we can evaluate the response of the entire TPC system to any given input. The TPC measurement can be thought of three different systems each which introduce errors and or biases into the final reconstructed tracks; the software, the detector, and the experimental setup. The

There are several effects in a complex experimental set up that influence the data in either unknown or un-quantifiable ways. One such effect is the bias of the triggering system, here the Kyoto and Katana multiplicity and veto arrays preferentially select data that is emitted in a particular reaction plane. As previously discussed saturation effects in the electronics, notably the shadowing of other tracks. The effects of track multiplicity and the distribution of heavy ion and residues from the breakup of the target and projectile. One could propose to make a simulation or investigation into each individual effect in order to make a full MC simulation of data and study the response

of the detector this way. Though great care was taken in developing an accurate MC simulation, like all models there are assumptions and simplifications that were made. Simply put, there is no better substitute for experimental data than itself. By embedding MC tracks into experimental data – and propagating through the tracking and reconstruction algorithm – one can account for all these sources of biases which are contained in the experimental data, while at the same time measuring the response of the TPC.

As discussed in Section 1.1, the software is composed of several tasks, each of which have the possibility of introducing errors or biases through assumptions made in the tracking algorithm. The detector system introduces errors related to the physical measurement itself which can be addressed through modeling the TPC, and its materials.

For all of the sources of biases in the TPC, it is clear that a MC type approach to solving for the response of the TPC would be the most practical method. Also by embedding MC events into real data we can take into account the effects of the experimental setup as well as the software and the detector system all together at once.

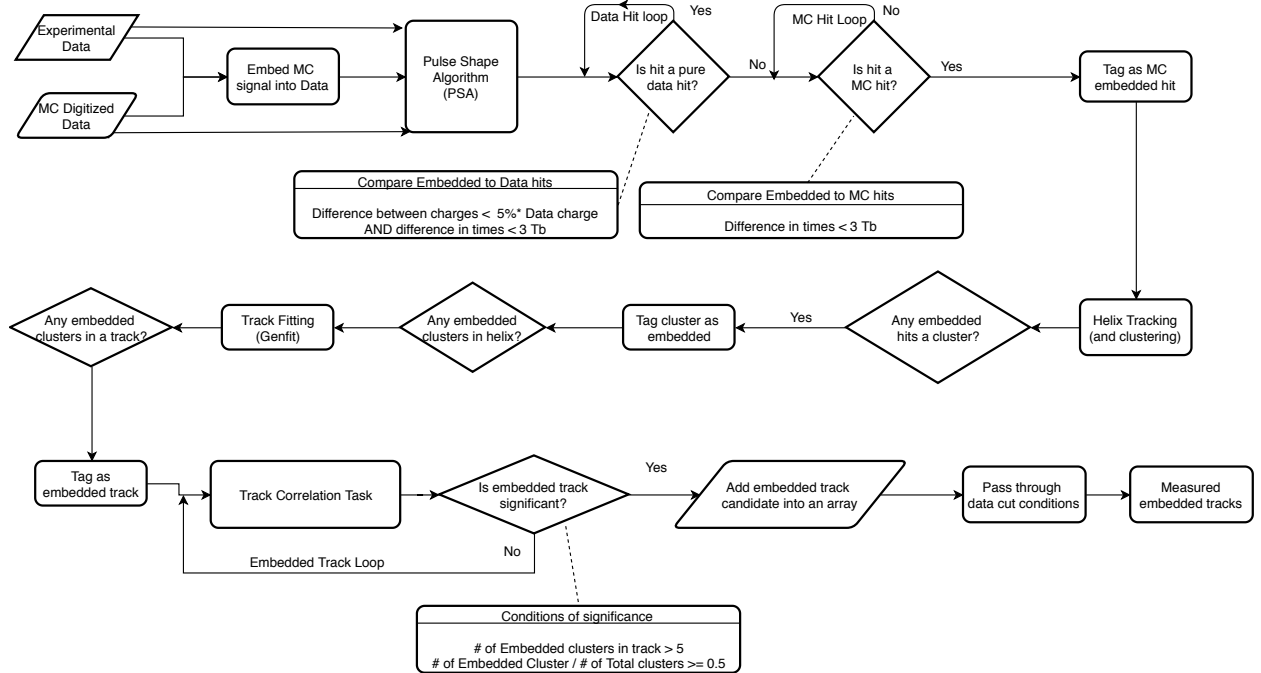


Figure 1.25: Flow of embedding implementation in the software.

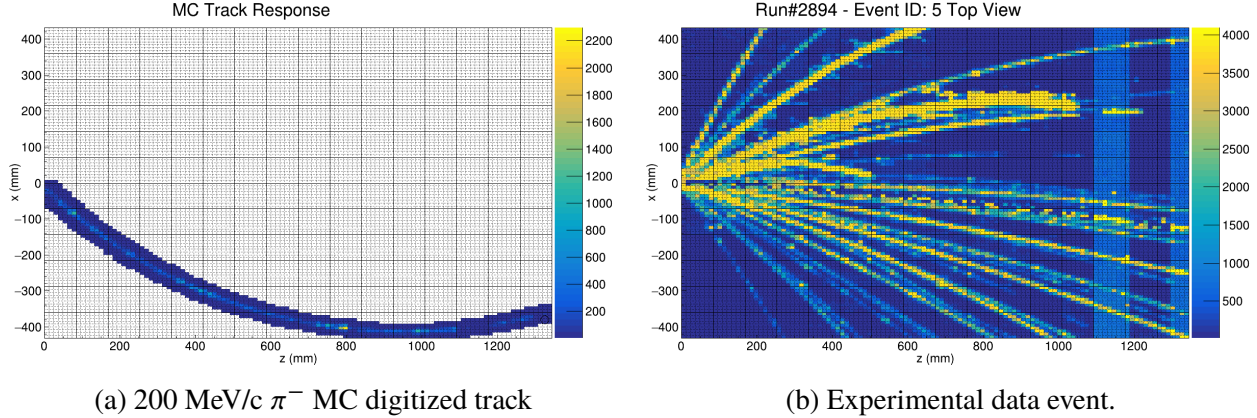


Figure 1.26: A 200 MeV/c π^- embedded into a nuclear collision type event. The embedded track identified by the software is highlighted by the solid green line.

The detailed flow diagram of the software implementation of embedding algorithm is shown in Fig. 1.25. Starting from Geant4 and passing through the 3 MC tasks described above, the output response of the MC track in the TPC is created. From here we directly embed the MC signals into data by adding the MC signals into the data time bucket spectrum, pad-by-pad. As described in Sec. 1.4.4, prior to embedding the MC signals, all pads which are saturated in the experimental data are identified and flagged. The MC signals are forbidden to be embedded after the MC saturation time bucket value. Figure 1.26a shows the response of a 200 MeV/c π^- track in the TPC; we have embed this track into the data event, Fig. 1.26b, just as an example. We will refer to experimental data with embedded MC signals as “embedded data” for short, the MC generated response as “MC data”, and data only containing only the experimental signals as “experimental data”. The three set of data are each independently analyzed by the PSA algorithm described in Section 1.1.4, which finds all the hits associated with each data set. From this the three independent hit data sets are temporarily stored.

Here within the PSA algorithm, is the first and most important part of the embedding software. The PSA task has the job to identify which hits in the embedded data set originate from the MC hits set and which are from the experimental data. Once the MC hits are identified, these embedded hits can be tagged and tracked through the entire software.

First, the hits in the embedded set are matched against the experimental data, identifying which

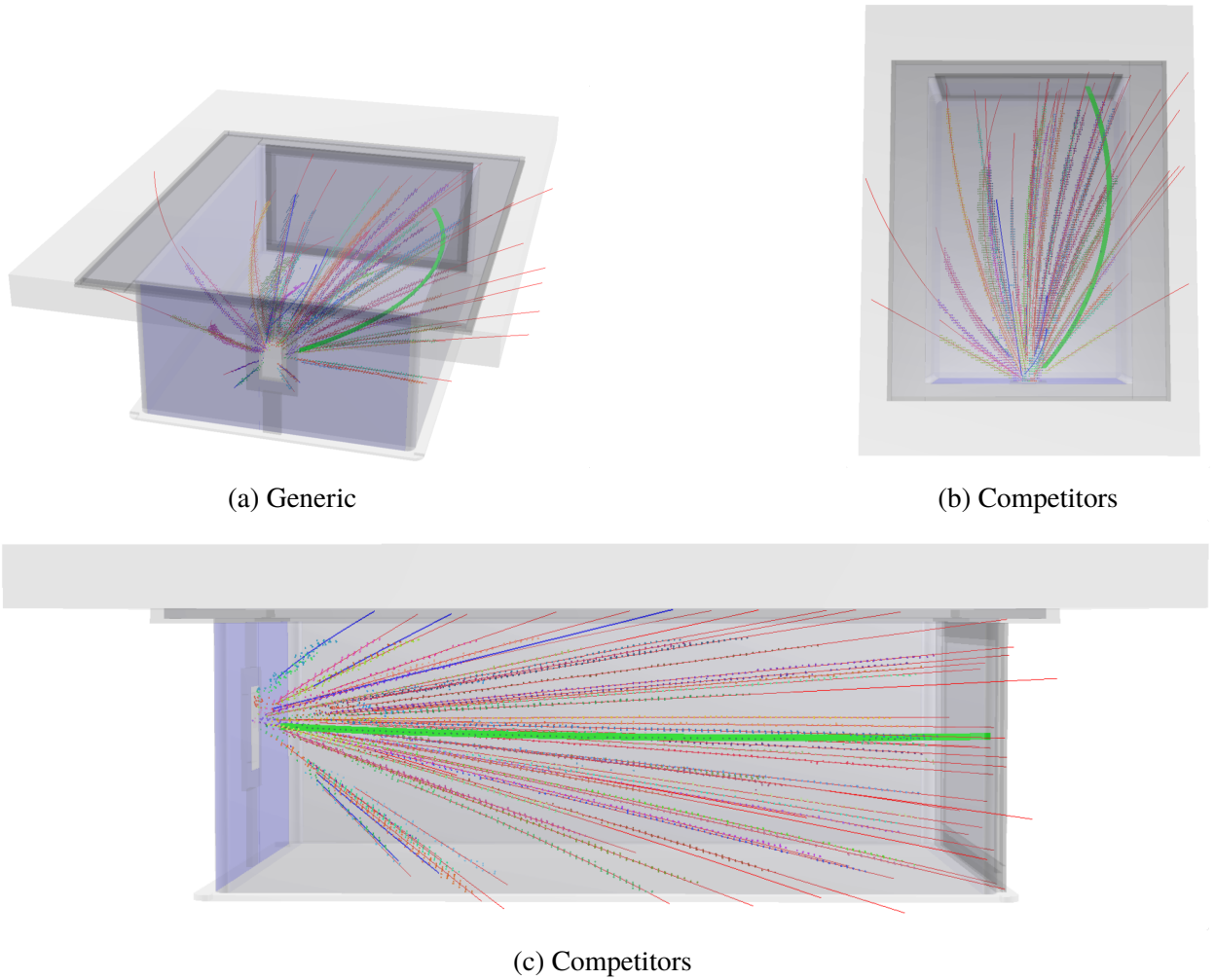


Figure 1.27: A 200 MeV/c π^- embedded into a nuclear collision type event. The embedded track identified by the software is highlighted by the solid green line.

of the embedded hits originate from the experimental hit set. For two hits to match, they must satisfy two criteria, $|Q_{\text{Data}} - Q_{\text{Embed}}|/Q_{\text{Data}} < .05$ and $|t_{\text{Embed}} - t_{\text{Data}}| < 3$ where Q and t represent the charge and time of the hit respectively. Hits that satisfy these criteria are then removed from the embedded data set.

The surviving hits are then compared with the MC hit data set, where the criteria for a matching MC hit is, $|t_{\text{Embed}} - t_{\text{MC}}| < 3$. There is no requirement for a matching criteria for the charge values which would artificially bias the charge values selected depending on our cut; which is critical for minimum ionizing particles such as pions. This can only be accomplished by first removing almost

all of the experimental hits as was done in the first step. Each embedded hit that passes this step of criteria is tagged as a originating from a MC hit. From here, the embedded data is treated as if it were real data passing through the same software analysis.

If a helix track has one hit that is embedded it will also be tagged as embedded. When the hits in a helix track are clustered, if a cluster contains one embedded hit it is itself tagged as an embedded cluster. Furthermore, if a track that is reconstructed contains any embedded clusters, it is tagged as an embedded track. The goal of this naïve tagging approach is to preserve all the information of where the embedded hits, clusters, and tracks have gone, preserving as much information until the end without introducing a bias.

It is the job of the embedded correlation task to identify which of the final embedded tracks are candidates for the original input track. For example, several things may happen along the process of embedding that may disqualify a track as a candidate in this naïve tagging. A track could break up, lose or share its charge with and adjacent track; it may be not be identified at all for a variety of other reasons. For the embedded track to be a candidate of the input MC track, it must satisfy two conditions, $N_{\text{sat}} > 5$ and $N_{\text{sat}}/N_{\text{Total}} \geq .5$, where N_{sat} is the number of saturated clusters in a track, and N_{Total} is the number of total clusters. The first criteria is a simple minimum cut where to ensure the minimum condition of a embedded track is met at least having 5 clusters. The second criteria is the strongest cut, ensuring the track has at least half of its clusters coming from embedded MC signals. The set of tracks which satisfy both conditions are saved into an array of candidate tracks. In this way the user can decide how to sort these tracks for studying either efficiency or track splitting.

If the embedded track is split into multiple tracks, the user must select what they believe to be the track which most represents the original track, for the purposes of calculating efficiency. Typically only one of the tracks in the set will satisfy one of the reasonable quality cut conditions in an analysis. For example the most reasonable assumption is the track originating from the vertex is the most correct in this case, where as the split fraction of the track wont originate from the vertex but instead have a large distance to vertex value. In this thesis, the track with the minimum distance

to vertex is identified as the track in which the efficiency analysis will be performed.

1.5.1 MC and Data Comparison

Here we compare several important observables to ensure the MC is simulating the data. These observables will be relevant for the quality cuts and efficiency analysis discussed in Section 1.8. The most important observable is the total number of clusters. The number of clusters in a track depends on the geometry of the TPC, the spherical angles of the track, and the clustering algorithm. MC tracks were embedded into data for several particle types; the input angular and momentum distribution was uniform and the final distributions were weighted such that the angular and momentum distribution matched that of the data for a fair comparison. Figure 1.28 shows the normalized cluster distributions for the MC and data for several particle types. There is no data below 20 clusters because this is the minimum cut to ensure quality PID lines in the data. The normalization is changed for each particle type to display them on the same scale. Very good agreement is seen between the MC and data over a wide range of particle species.

The second most important observable is the distance to vertex. Figure 1.29 shows the distance to vertex distributions for the MC embedded tracks and the data for the same range of particle species. The distributions were again normalized to different values to display on the same scale. Both data sets here are track number of clusters > 20. It is also worth mentioning the data plotted is also after the space charge correction. Before the space charge correction the distributions would be much wider. Since we correct for the space charge in the data we compare here to the embedded MC without any space charge effects, making a fair comparison.

We can see good agreement between the MC PRF for π^- in Figure ??, and the data PRF, Fig. ??, where the black line is the PRF fit to the experimental data. It is sufficient to use such a simple universal PRF function as we can describe all the crossing angle effects discussed in ???. Therefore these effects must arise from geometric effects related to the track angle, the amount of charge distributed over an anode wire, and the superposition of the PRF from neighboring anode wires which contribute to the appearance of a changing PRF.

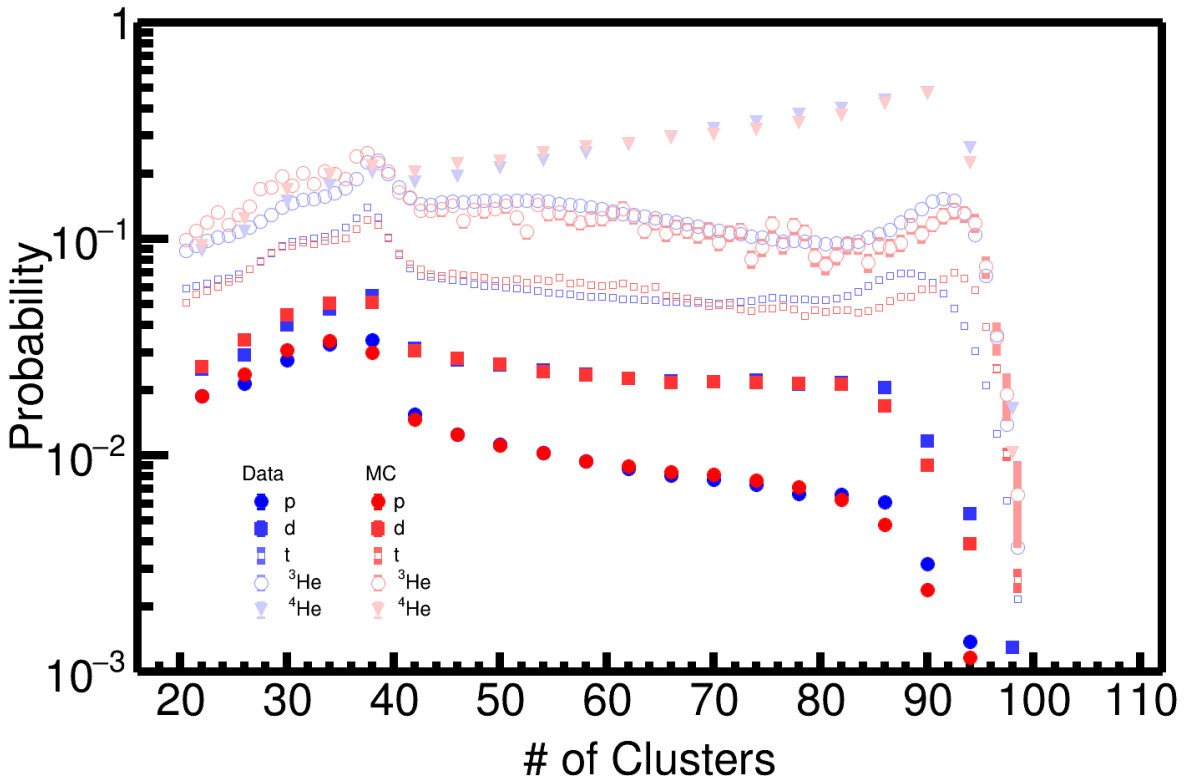


Figure 1.28: Comparison of MC to data.

Add Figure of dE/dx MC vs Data Add Figure of Momentum resolution MC vs Data Add Figure of track residuals? MC vs data?

1.6 Aligning TPC

1.7 CoBo timing correction

The arrival time of signals originating from each pad may differ due to timing delays in the electronics and cabling. The timing differences will affect the y-position measurement of each track. The y-residuals reveal that the timing differences correspond to about ± 2 mm in position differences. The timing difference is stable for each pad across several runs.

Figure ?? shows the y-residuals, across all the rows, for three different layers. Before the correction one can see large deviations in the y-residuals which correspond to timing differences.

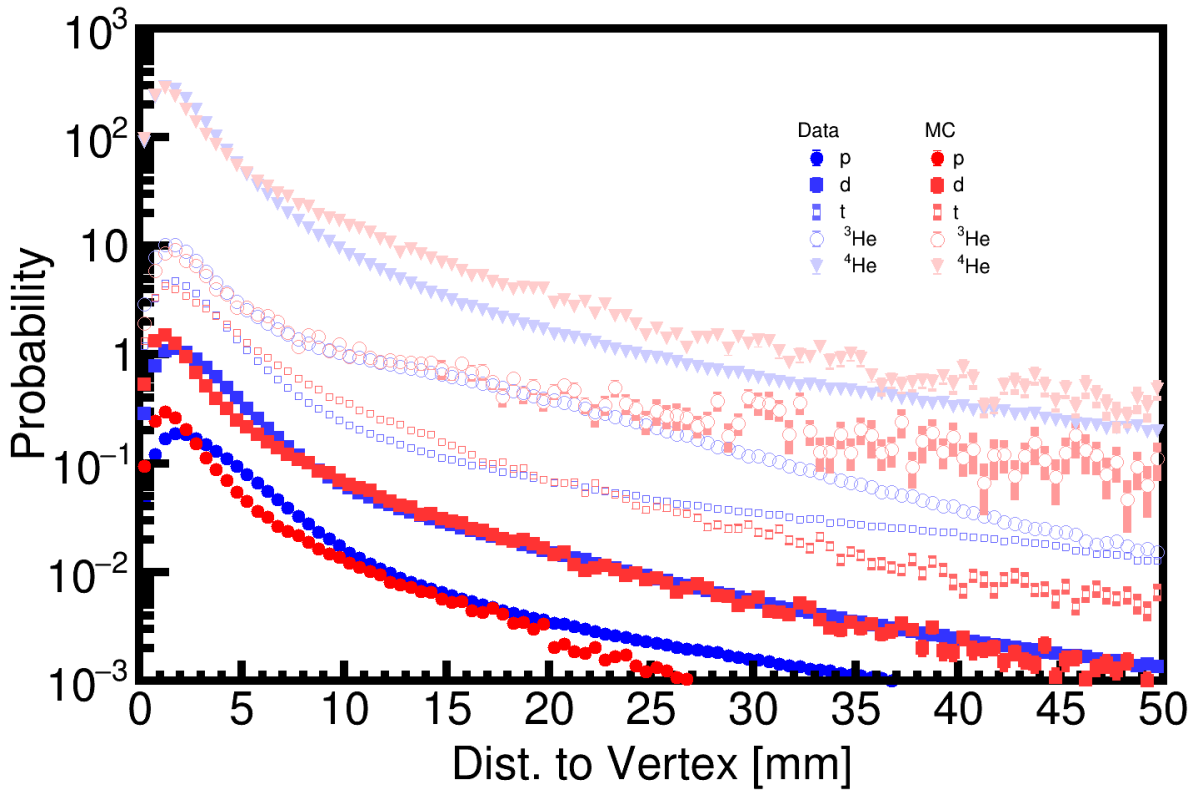


Figure 1.29: Comparison of MC to data.

The mean value of the y-residual distribution is fitted and a map is constructed for each pad. The data is then reconstructed subtracting the value of that map, dy , for each pad. The resulting corrected distribution is shown in Fig. ?? for the same layer set. Figure 1.32 also show the summary of all the pads before the correction and after the correction. There is a significant improvement in the width of the distribution going from 1.5 mm to 0.6 mm.

1.8 Efficiency Corrections

Add Figures of efficiency vs angles in TPC polar angle plot for pions

Since the S π RIT TPC is a fixed target experiment it's angular coverage is certainly not 4π . Because the target is several cm away from the widow of the field cage the geometric acceptance is not even 2π . The rectangular design complicates the calculation of the geometric acceptance, or the efficiency. Because of this there are regions of the TPC where it is impossible to reconstruct a

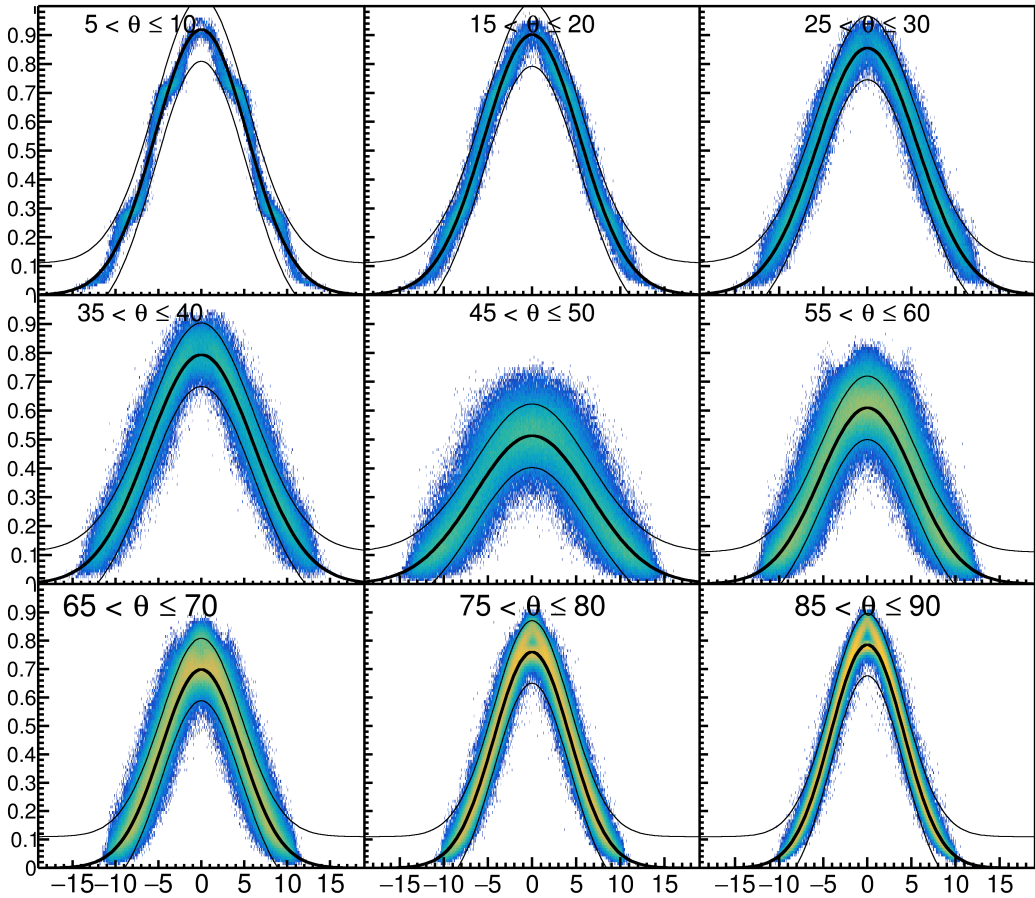


Figure 1.30: PRF response of Monte Carlo simulation of π^-

track due to the geometric in these regions the efficiency is exactly 0. In the regions of non-zero efficiency, the efficiency is a function of at least three main parameters that define the phase space of a track, momentum p and the two spherical lab angles θ_{Lab} and ϕ_{Lab} .

The track efficiency ϵ is calculated bin-by-bin and is simply written as,

$$\epsilon = \frac{n_{reco}}{N}, \quad (1.13)$$

where n_{reco} is the number of embedded tracks which are successfully reconstructed, and N is the total number of input embedded tracks for that given bin. A track is defined to be successfully reconstructed if it exists in the correlation task described in 1.5, and therefore meets the minimum criteria for an embedded track, and if it passes the various quality cuts performed on the experimental

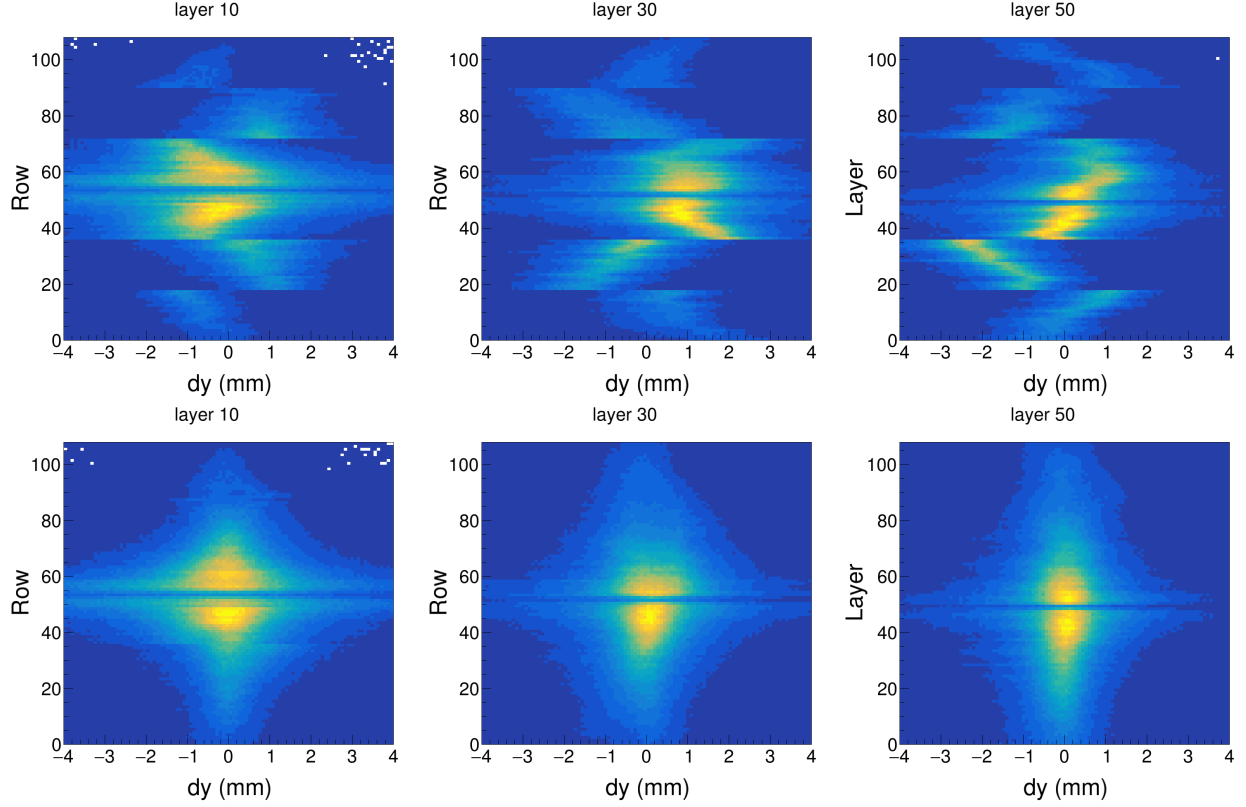


Figure 1.31: TBW

data set; this could be angular cuts, PID cuts, etc. The TPC response will introduce a finite resolution in both the angles and the momentum. Because of the final measured track could have migrated out of the input bin into another bin. The bin-by-bin correction method is only valid if this effect is small as compared with the size of the bin. If not a more complicated un-folding procedure is needed. The efficiency is defined as the number of all tracks that were reconstructed and passed the cuts successfully, even if some had migrated to other bins, the efficiency value is assumed to represent the center of the input MC bin.

Single MC tracks are embedded into a set of 10^4 on target events and the measured output tracks are correlated to the input track from the embedding software. If the track split in the analysis software, and there are several tracks identified by the software as an embedded track, or part of one, we certainly cannot double count the track as the efficiency is defined strictly as $\epsilon < 0$. In this case, the track with the minimum distance to vertex is taken for the purposes of calculating

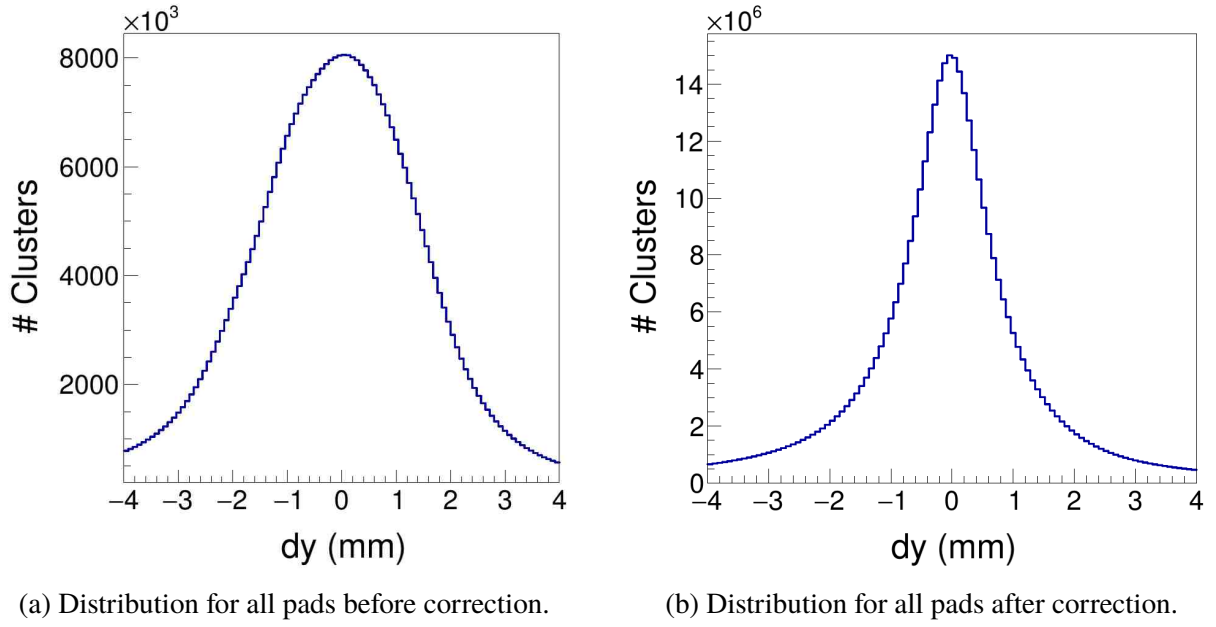
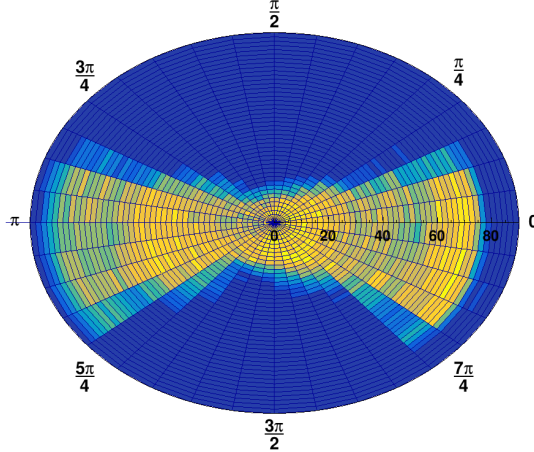


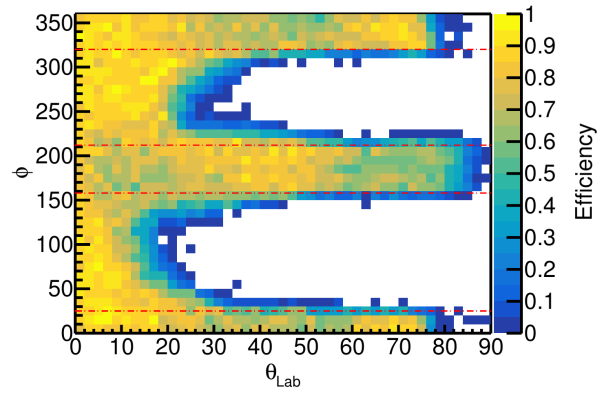
Figure 1.32

efficiency. This is because in the case the track splits, it is very rare for the later segments of the track to have a distance-to-vertex which originates from the target region. It's reasonable to assume the track with the minimum distance to vertex is the track that best represents the "real" track. The embedded MC tracks are generated as a uniform distribution in θ, ϕ , and p , to ensure each bin has as similar number of input tracks N , giving approximately the same statistical error. Here the efficiency distribution is independent of the initial input distribution since we were careful to not assign tracks that migrated out of the input bin, into another bin, which would make the efficiency biased by the input distribution.

Figure 1.33 shows the efficiency calculated for π^- tracks traveling with momentum $200 \text{ MeV } c^{-1}$ as a function of the two laboratory angles. It is easiest to visualize the efficiency distribution first in a polar representation which is most like viewing the actual TPC progressing to a visualization that is easier to see the values. Figure 1.33a shows the efficiency values plotted in a polar representation where θ_{Lab} is represented as the radial dimension and ϕ is represented as the polar angle. This way is best understood as if one looked at the TPC from the downstream point of view. Of course the vertical direction of the TPC, $\phi=90^\circ$, is limited in vertical space, therefore tracks are not



(a) Polar efficiency plot where θ is represented by the radius of the circle and ϕ is measured as the polar angle made between the y and x axis; this view is best understood as looking at the TPC from the downstream point of view.



(b) Flattened angle plot

Figure 1.33: Efficiency calculations for π^- particle traveling at 200 MeV c^{-1} .

reconstructed well. The same is the case in downward going tracks, the region centered around $\phi=270^\circ$. The best regions are seen by the high efficiency values which are left and right in the TPC where the rectangular TPC has the highest acceptance. Though this view is the most intuitive to think about in a physical geometry sense, the values of the efficiency in each bin are difficult to see. Figure 1.33b shows the same efficiency plot but plotted in a more standard two dimensional plot. Here we can see even better the acceptance of downward going tracks, $\phi=270^\circ$, is greater than the dip in upward going tracks, $\phi=90^\circ$, due to the field cage being centered in the magnet and not in the TPC.

The area enclosed by the red lines represent the region of the highest efficiency over the full region in θ_{Lab} . Since we take cuts similar to these in the real data, we assume the efficiency is independent of ϕ over these small regions. The efficiency then can be represented as just a function of the two remaining variables. Figure 1.34 shows the efficiency of π^- and π^+ particles in the $^{132}\text{Sn} + ^{124}\text{Sn}$ system and Fig. 1.35 for the $^{108}\text{Sn} + ^{112}\text{Sn}$ system as a function of θ_{Lab} and momentum p_{Lab} .

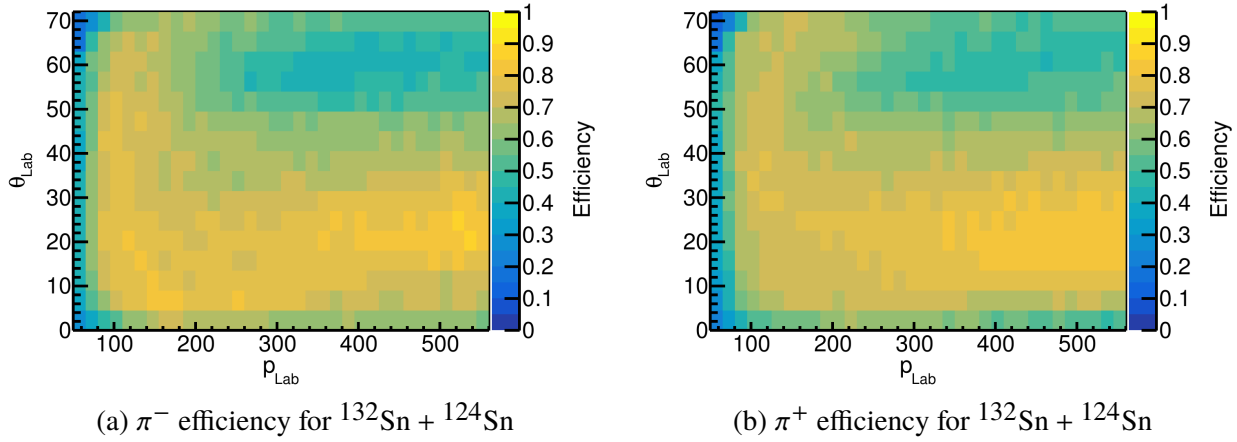


Figure 1.34

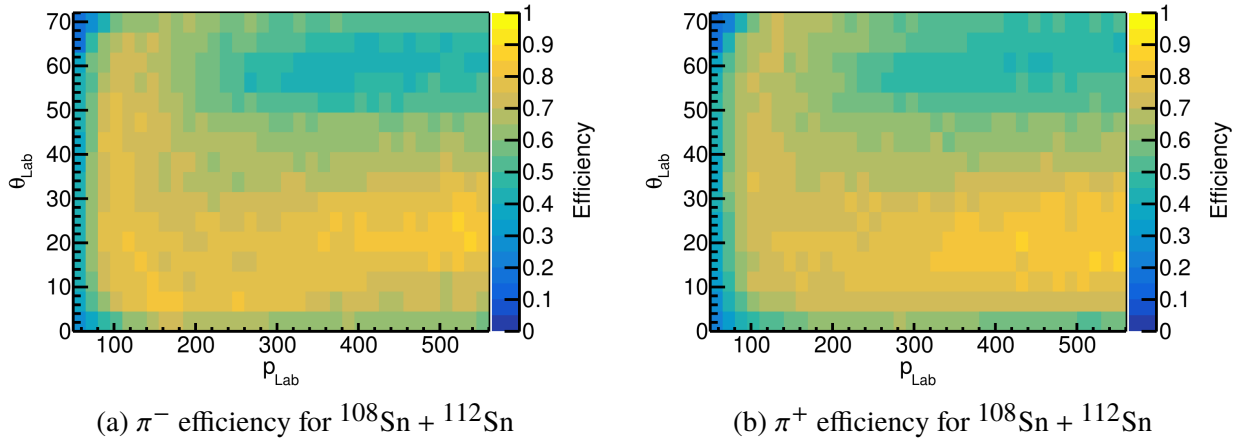


Figure 1.35

The efficiency correction is applied track-by-track, where the efficiency of the i -th track ϵ_i is retrieved from the database. The correction factor C_i is defined as,

$$C_i = \epsilon_i^{-1}. \quad (1.14)$$

The track is then weighted by the factor C_i when plotting in any type of graph for any observable.

CHAPTER 2

DATA ANALYSIS II

2.1 Radio Isotope Beam Factory (RIBF) Facility

The primary and secondary beams were produced at the Radioactive Isotope Beam Factory (RIFB) facility at RIKEN, in Wako-shi, Japan. The RIBF facility starts with two primary beam types, ^{132}Xe and ^{238}U , which are produced by an ion-source and accelerated to progressively higher kinetic energies by 1 linear accelerator (RILAC), and 4 different cyclotrons (RRC, fRC, IRC, and SRC), until they reach a beam energy of 345 MeVA. Figure 2.1 shows the later stages of the cyclotrons and the following beam lines they feed into.

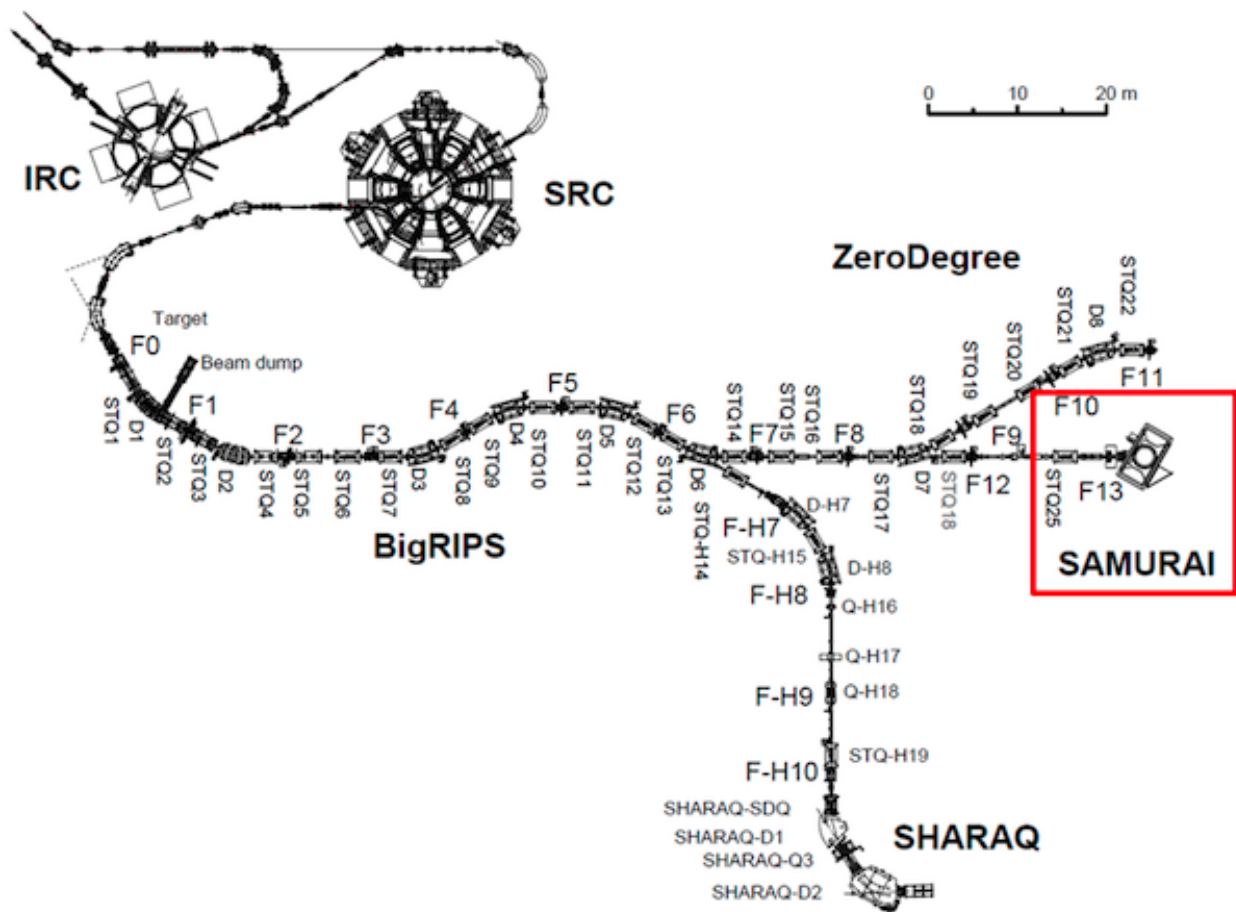


Figure 2.1: Overview of the RIBF, BigRIPS, and SAMURAI beamline.

Primary Beam	Secondary Beam	Energy at mid target MeVA	Intensity kHz	Purity (%)
^{238}U	^{132}Sn	269.2	9.5	54
^{238}U	^{124}Sn	270.3	9.1	10
^{124}Xe	^{112}Sn	270.4	7.6	48
^{124}Xe	^{108}Sn	269.3	7.5	52

Table 2.1: Primary and secondary beam properties produced in the S π RIT TPC experimental campaigns.

After the SCR, the primary beams impinge on a rotating 3 mm Be target which produces many different species by fragmentation. These fragments are then separated by the BigRIPS spectrometer which is tuned to the particular secondary fragment of interest. This is accomplished through several dipole magnets, slits, and wedge degraders. The resulting secondary beam is not pure and the purity depends on the capability of BigRIPS to deliver the secondary beam of choice and the primary beam used.

In these set of experiments several beams were produced with varying intensities and purities. Table 2.1 summarizes the average qualities of the 4 secondary beams produced in the two experimental campaigns where most beams were delivered with an intensity of 10 kHz.

2.2 Beam Particle Identification

The secondary beam is produced through the projectile fragmentation of the primary beam off of a 3 mm thick, rotating Be target [9]. The resulting fragments are filtered in-flight to the desired secondary beam. The in-flight separation is handled by the BigRIPS fragment separator which is shown in Fig. 2.1. The dipole magnets D1 and D2 act as a velocity filter, selecting on certain magnetic rigidities $\beta\rho$. Several sets of slits further purify the secondary beam quality by throwing away particles which do not focus on the right focal planes. These are the areas where the particles with different velocities focus to different locations in space, which occur at F3,F5, and F7 positions. Each beam is tracked with the remaining part of the BigRIPS spectrometer tracking system. The

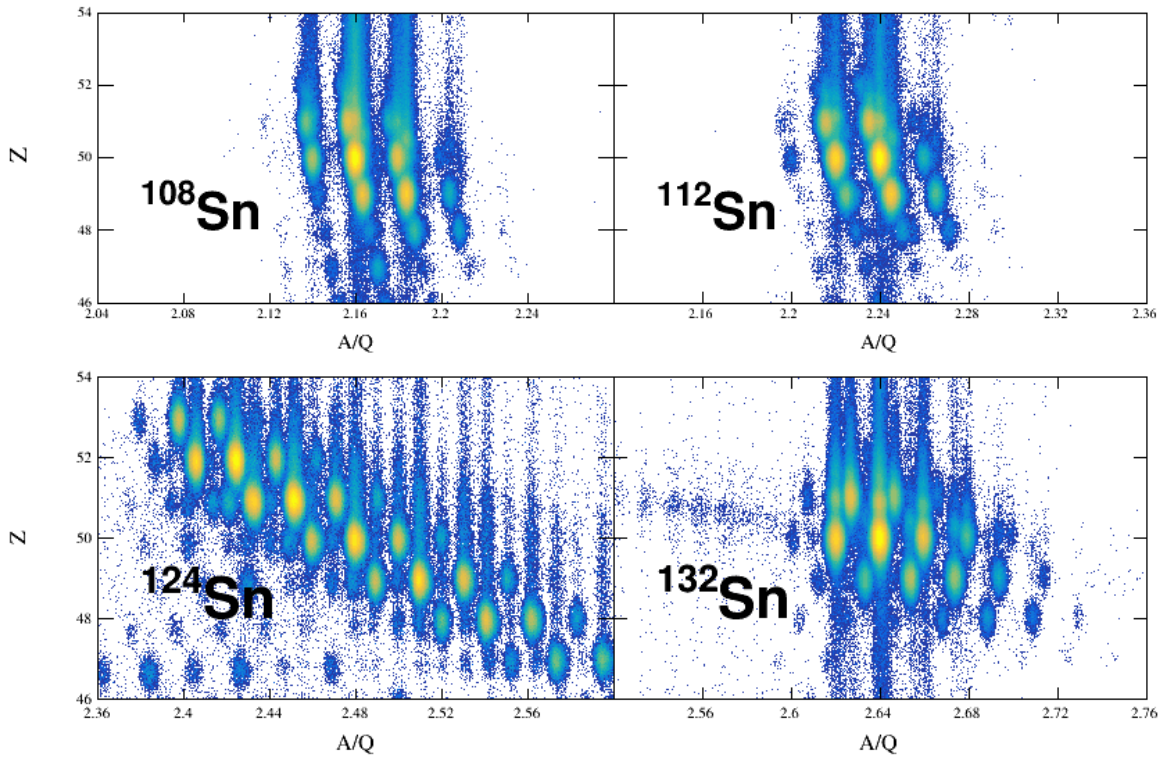


Figure 2.2: Overall beam PID for all the systems. Several contaminants other than the desired secondary beam can be seen.

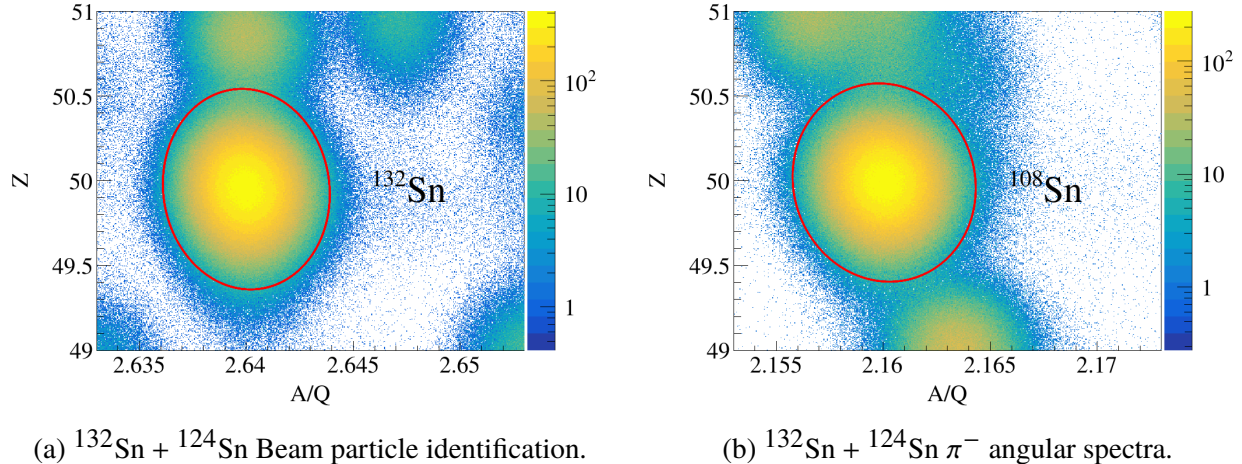


Figure 2.3: $^{108}\text{Sn} + ^{112}\text{Sn}$ Beam particle identification.

particle identification of each beam is achieved by the TOF- $B\rho-\Delta E$ method described in [10], where the Time of Flight (TOF) information is given by the time it takes to cross two plastic scintillators at

F3 and F7 focal planes, and the ΔE information is given by the Multi-Sampling Ionization Chamber (MUSIC) [11]. From this method the atomic charge, Z , and mass to charge ratio, A/Q , of each particle was measured and separate species represent two-dimensional Gaussians in this space.

Figure ?? shows the beam PID for all the systems for events which satisfied the trigger, several contaminants other than the desired secondary beams still passed through the BigRIPS spectrometer and made it into the TPC. The beam purity of each desired secondary beam is listed in Table 2.1. The desired secondary beam of interest can be selected by using an appropriate gate around the corresponding group, since the BigRIPS PID resolution is good enough to separate separate beam types. Each particle gate is selected by fitting a multivariate normal distribution with two variables defined as,

$$f(x, y) = \frac{1}{2\pi\sigma_x\sigma_y\sqrt{1-\rho^2}} \exp \left\{ \frac{-(x - \mu_x)^2/\sigma_x^2 - (y - \mu_y)^2/\sigma_y^2 + 2\rho xy/\sigma_x\sigma_y}{2(1 - \rho^2)} \right\}, \quad (2.1)$$

where $x=A/Q$, $y=Z$, μ is the mean values, and σ are the Gaussian widths of the two variables. The gates drawn in Fig. 2.3 are summarized in Table 2.2.

Particle Type	$\mu_{A/Q}$	$\sigma_{A/Q}$	μ_Z	σ_Z	ρ
^{132}Sn	2.64	0.0014	49.95	0.209	-0.052
^{108}Sn	2.16	0.0015	49.99	0.207	-0.059

Table 2.2: Multivariate normal distribution fit parameters for four beams.

Figure 2.3a shows a zoomed in view of the PID centered around the ^{132}Sn beam and Fig. 2.3b the ^{108}Sn beam. The red lines represent the cut where particles identified inside the circle represent the beam events which are identified as the good beam events. For both ^{132}Sn an ^{108}Sn a 2.83σ cut is taken around the mean values.

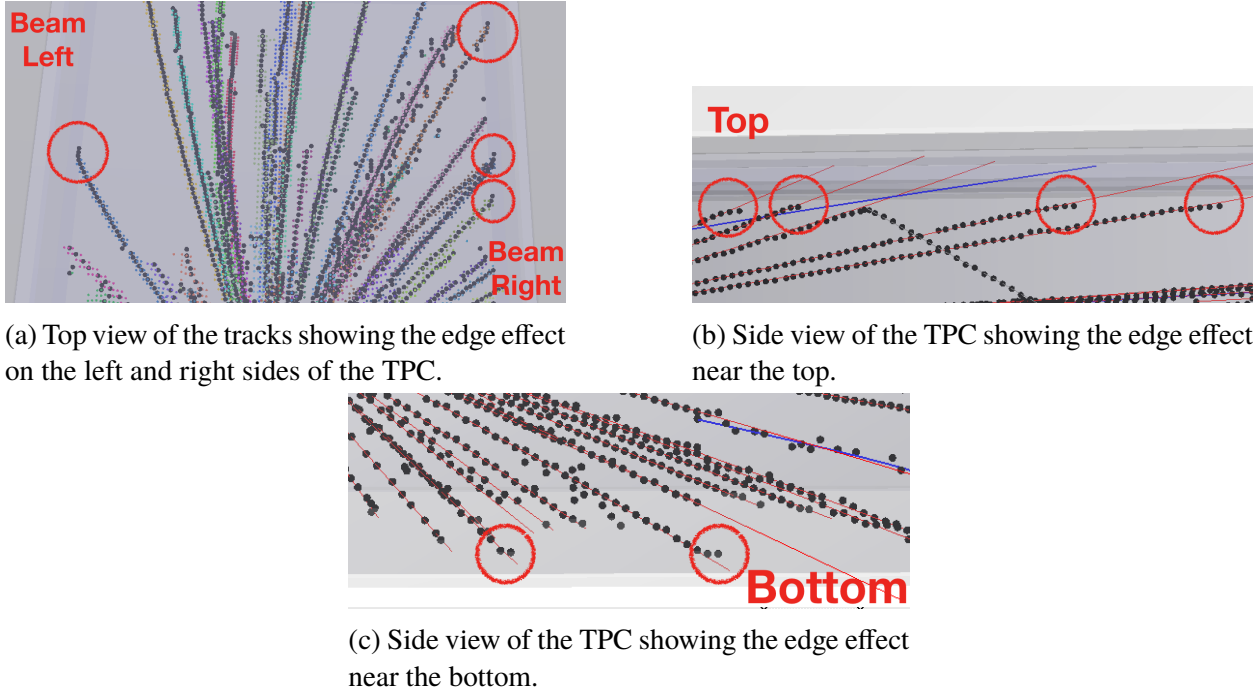


Figure 2.4

2.3 Edge Cuts

Near the edges of the detection volume, the clusters of tracks significantly deviate from the trend of the fitted track as seen in different view of the reconstructed clusters in Fig. 2.4. This effect comes from an edge effects where the last pads on the edges of the pad-plane have no neighboring pads containing charge, and therefore the last pad, or in the case of the vertical time bucket spectrum, represents the last known position of the collected charge. In this case the cluster position is biased towards the inside of the TPC. While the number of affected clusters is small as compared with the total number in the track, but the deviation at the end of the track is enough to start causing issues in the momentum reconstruction. Simple cuts were taken to graphically remove these clusters around the left,right, top, and bottom of the TPC. The hits that were cut out satisfied the following conditions,

$$|x| \geq 420 \text{ mm}, \quad y \leq -522 + y_0 \text{ mm}, \quad \text{and} \quad y \geq -64 + (\text{Hit Shift}) \text{ mm}.$$

2.4 High Density Cut

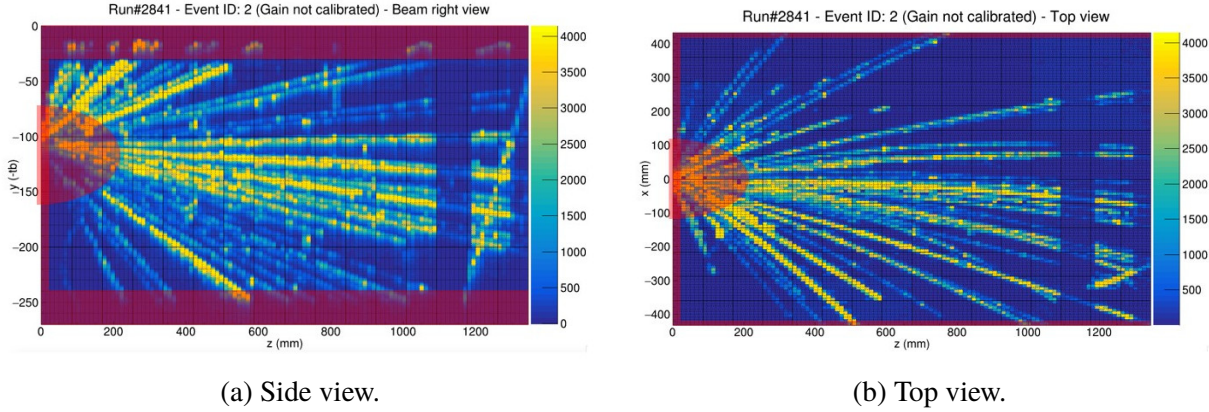


Figure 2.5: Views showing the high density and edge cuts.

The high track multiplicity in each event is quite high and since the tracks all originate from a common vertex, the density of tracks near the target region is very high. In this region the track separation is too small for the software to correctly determine and sort the charge information into the appropriate track. The information provided by extra vertex point from external BDC tracking described in ??, provides all the information about the vertex location. The bad quality of hit information near the target region only hurt in the tracking and PID of a track. Hits lying within an semi-ellipsoidal cut around the target are removed from the software and not included in the track and momentum reconstruction. Figure 2.5 shows the extent of the ellipsoidal cut in the high density region, along with the edge cuts as shaded red regions in both views of the TPC.

2.5 Beam angle selection

The incoming secondary beam is deflected by the magnetic field and impinges on the target at some small but significant angle. From the BDCs tracking information, the beam is projected as a straight line right up until entering the magnet. The beam is then propagated through the magnetic field using a Runge-Kutta integration until reaching the target position. The beam angle on target can be categorized by two angles $\theta_{a_{proj}}$ and $\theta_{b_{proj}}$ defined as,

$$\theta_{a,\text{proj}} = \tan^{-1} \frac{p_x}{p_z}, \quad \theta_{b,\text{proj}} = \tan^{-1} \frac{p_y}{p_z}, \quad (2.2)$$

where p_x , p_y , and p_z are the components of beam momentum vector.

System	$\mu_{\theta_{a,\text{proj}}}$	$\sigma_{\theta_{a,\text{proj}}}$	$\mu_{\theta_{b,\text{proj}}}$	$\sigma_{\theta_{b,\text{proj}}}$
$^{132}\text{Sn} + ^{124}\text{Sn}$	0.61	2.94	-44.18	1.96
$^{108}\text{Sn} + ^{112}\text{Sn}$	-0.42	1.95	-55.17	0.97

Table 2.3: 2D Gaussian fit parameters for ^{132}Sn , ^{112}Sn and ^{108}Sn beam angle.

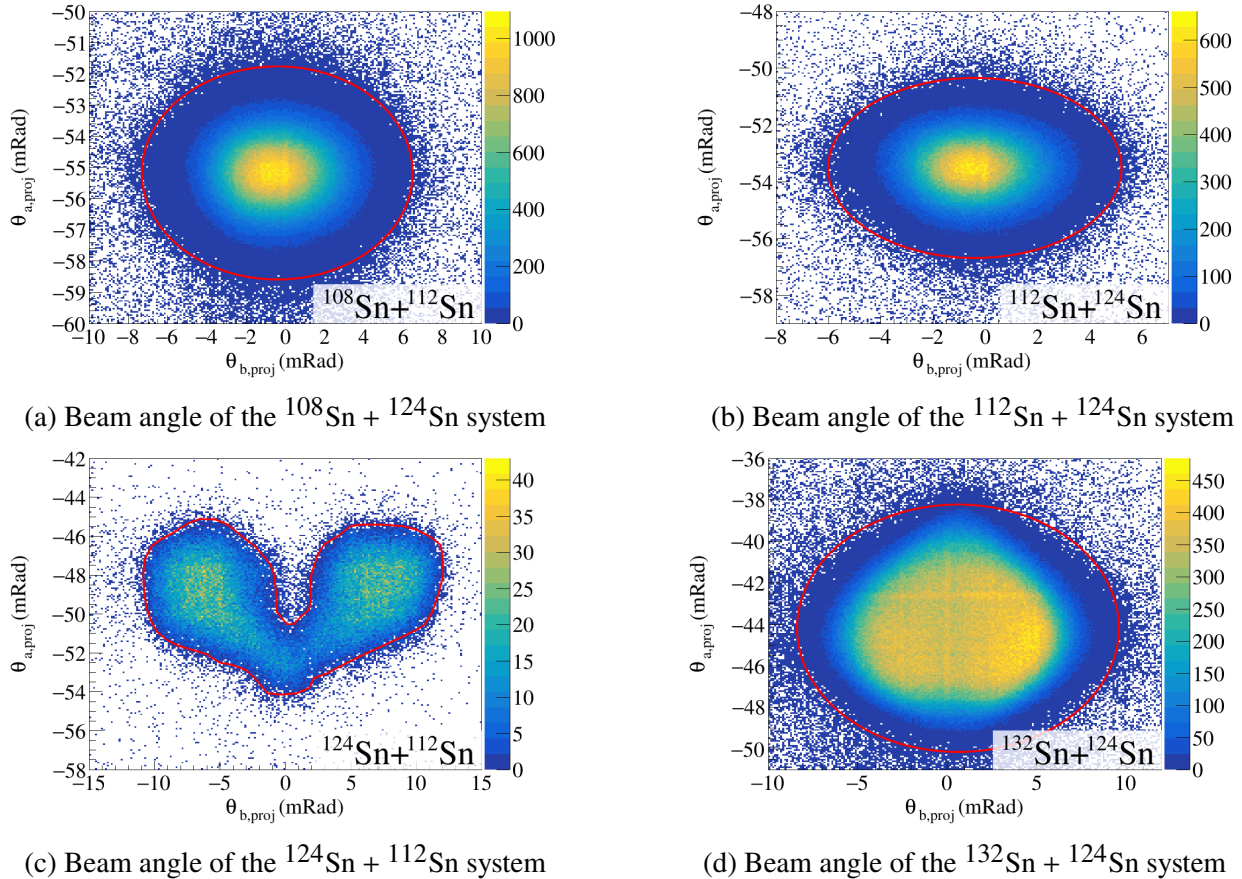


Figure ?? shows the distribution of beam angles for ^{132}Sn and ^{108}Sn systems. Graphical cuts represented by the red lines where events lying in the cuts represent beams that were reconstructed correctly by the beam tracking software outlined in [12]. Helping to eliminate some of the poorly reconstructed beam events.

2.6 Vertex Cut

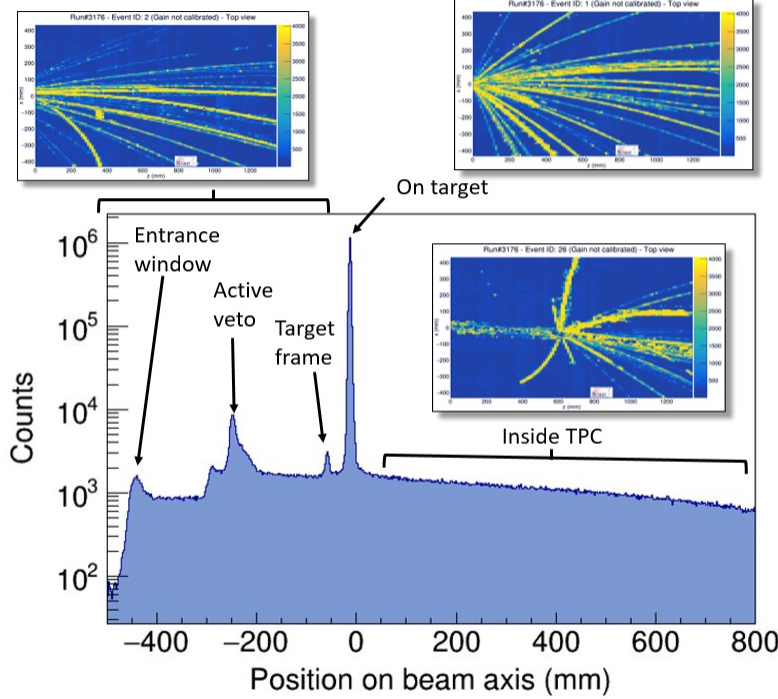


Figure 2.7: Projection of the vertex onto the z-axis.

The vertex information of an event, described in ??, is estimated from reconstructing the tracks of an event to one common source. The secondary beam encounters several solid and gaseous materials where a nuclear reaction can occur anywhere along the beam line. Figure 2.7 shows the z component of the reconstructed vertex for all events in the ^{132}Sn system. Several peaks are seen in the spectrum which correspond to several dense materials in the beam line such as the entrance windows, target frame, Active Veto, with the largest peak representing the target. Also collisions happen with the detector gas inside the TPC volume which are typically called active target events. To ensure that the secondary beam is really on the target of choice we perform a vertex cut around where we believe the vertex location of the target to be.

The target position was measured to be -13.2 mm . The z-component of all runs in each beam type are plotted around the target region in Fig. 2.8. The mean position of the vertex from the reconstructed data is around -14.76 mm which is about 1.6 mm off from the expected target

Vertex Resolution		
System	Mean (cm)	Sigma (cm)
$^{132}\text{Sn} + ^{124}\text{Sn}$	-14.79	1.2
$^{124}\text{Sn} + ^{112}\text{Sn}$	-14.71	1.1
$^{112}\text{Sn} + ^{124}\text{Sn}$	-14.78	1.2
$^{108}\text{Sn} + ^{112}\text{Sn}$	-14.75	1.3

Table 2.4: Summary of measured vertexes and their resolution.

position. The mean position for each system is listed in Table 2.4. Since the target thickness was less than 1 mm for all targets. Neglecting the small distributions in the thin target, the measured width of the vertex distribution can be interpreted directly as the vertex resolution of the TPC. The extracted vertex resolutions of each system are summarized in Table 2.4, with an average vertex resolution of 1.2 cm. The difference between the measured and actual target location is 10 times smaller than the intrinsic vertex resolution of the detector and is really and insignificant difference.

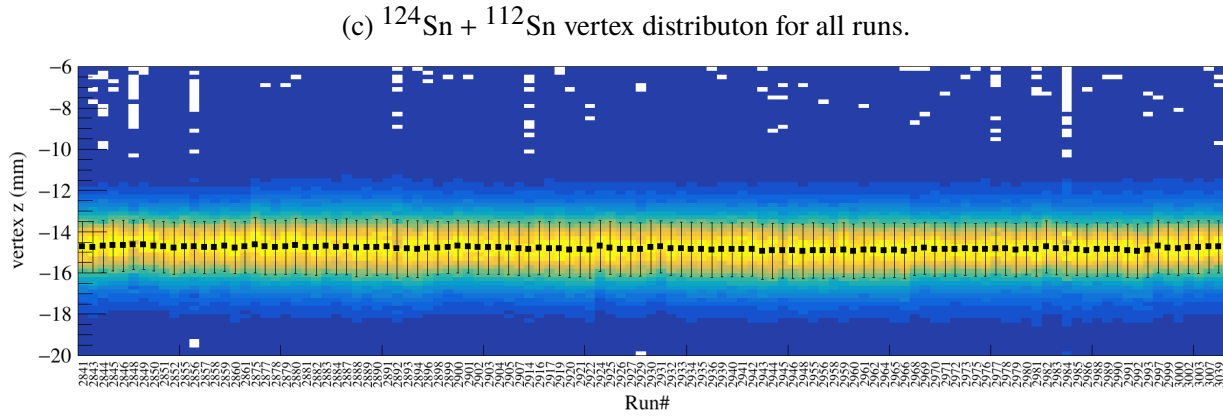
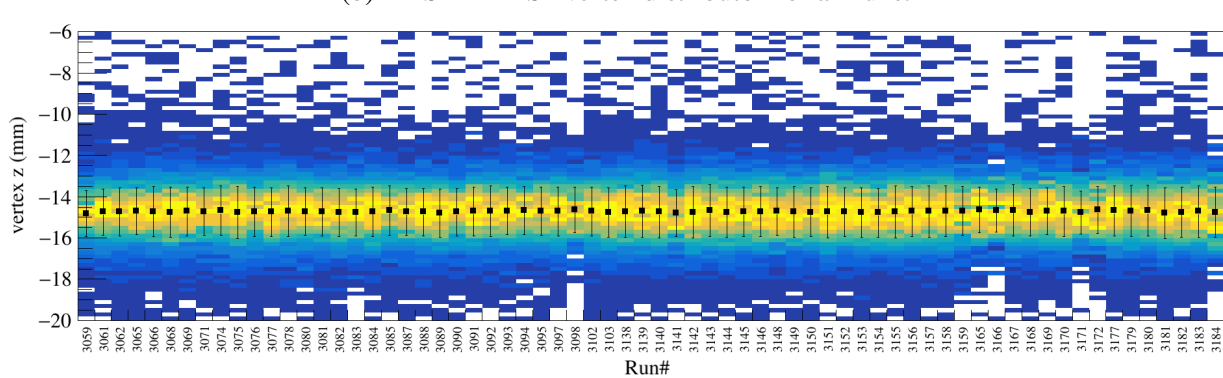
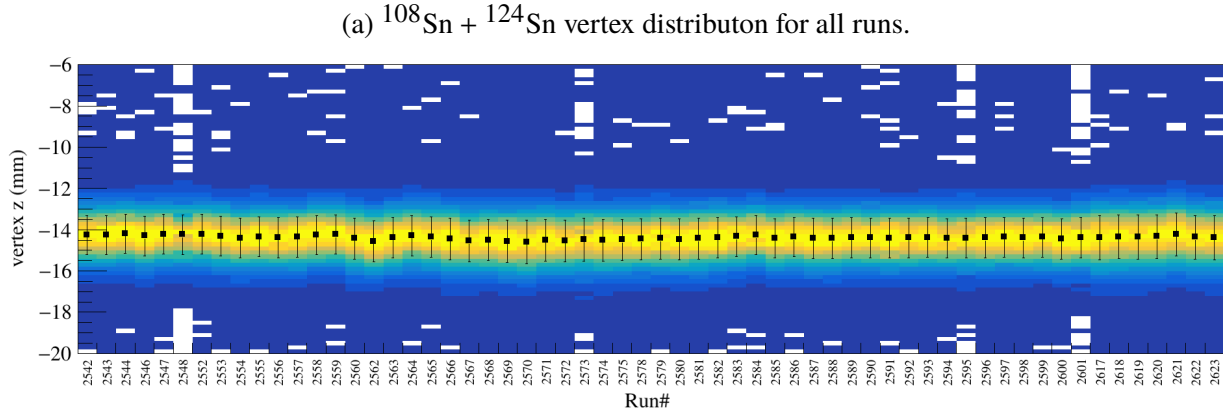
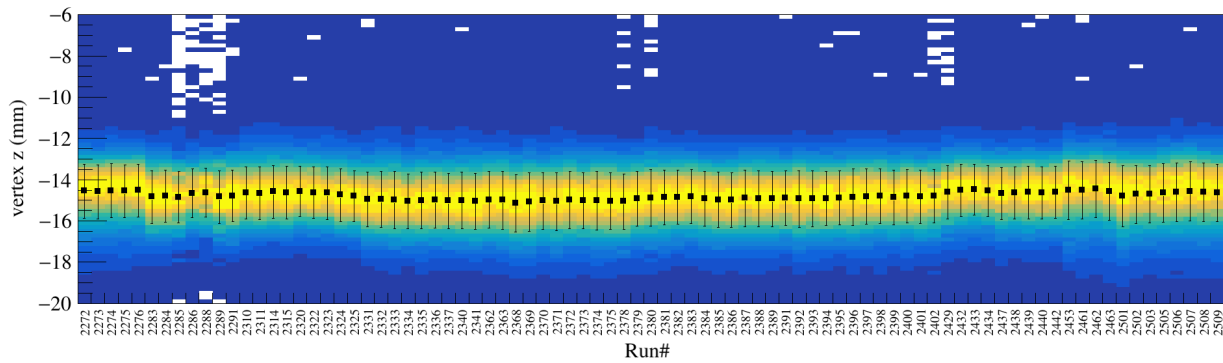


Figure 2.8

2.7 Impact Parameter Selection

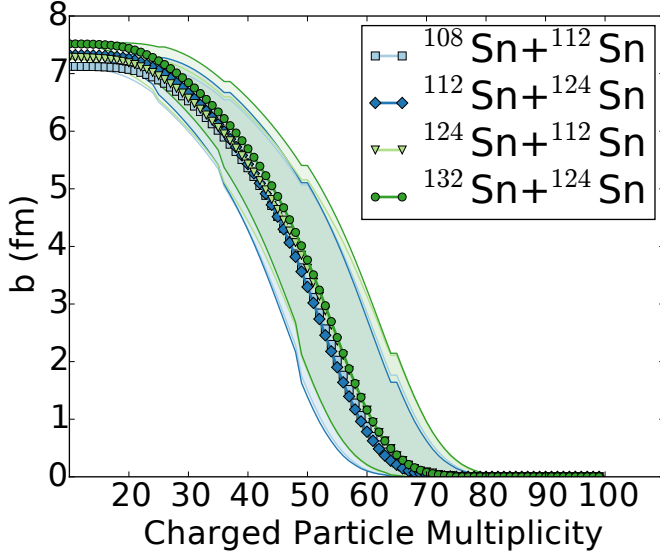


Figure 2.9: Estimate of the impact parameter from the track multiplicity.

The impact parameter is a theoretical quantity defined as the distance, between two centers of colliding nuclei. Though there is no way to directly measure the impact parameter in an experiment, the track multiplicity can be indirectly related to the estimated impact parameter of a collision [13]. As discussed in Section ??, the Kyoto multiplicity array was used to experimentally trigger on central nuclear collision events. This is under the assumption that as the number of charged particles produced in collision is related to the overlap region of the two nuclei. This is best described by a spectator-participant model of nuclear collisions, where a large fraction of the participating nucleons in the overlap region of the two colliding nuclei fragment into individual and clusters of nucleons. In the case where the impact parameter is zero, all the nucleons in both nuclei participate, were as larger impact parameters – more peripheral collisions – less nucleons participate.

The geometric cross section σ can be described as,

$$\sigma = \pi \cdot b^2, \quad (2.3)$$

where b is the impact parameter of the collision. If the track multiplicity of an event N_C is monotonically related to the cross section, the impact parameter can be written as a reduced impact parameter \hat{b} as,

$$\hat{b} = \frac{b}{b_{max}} = \int_{N_C}^{\infty} \frac{dP(N_C)}{dN_C} dN_C, \quad (2.4)$$

where b_{max} represents the maximum impact parameter detected by the TPC, b is the impact parameter of the vent, and $dP(N_C/dN_C)$ is the normalized multiplicity distribution [14]. The reduced impact parameter ranges from $\hat{b} = 0$ for the most central collisions and to $\hat{b} = 1$ for the most peripheral. A detailed analysis was performed, determining the maximum cross section σ_{max} , for each system, in which $b_{max} = \sqrt{\sigma_{max}/\pi}$. The detailed analysis is given in [12]. Figure 2.9 shows the estimated impact parameter for a given track multiplicity with the estimated error bands for each system.

In the $^{132}\text{Sn} + ^{124}\text{Sn}$ system the multiplicity cut was $N_C > 50$ corresponding to $\hat{b} = 0.4$ and $b = 3.1$ fm. For the $^{108}\text{Sn} + ^{112}\text{Sn}$ system the multiplicity cut was $N_C > 49$ corresponding to $\hat{b} = 0.4$ and $b = 3.1$ fm. These values were averaged over the multiplicity distribution as,

$$\bar{X} = \int_{N_C}^{\infty} X \frac{dP(N_C)}{dN_C} dN_C \quad (2.5)$$

where X can be the variables b , \hat{b} . In the $^{132}\text{Sn} + ^{124}\text{Sn}$ system the average $\hat{b} = 0.1 \pm 0.1$ and $\bar{b} = 3$ fm. In the $^{108}\text{Sn} + ^{112}\text{Sn}$ system the average $\bar{\hat{b}} = .1$ and $\bar{b} = 3$ fm. These quantities are useful when comparing to theory.

2.8 Track Quality Cuts

In this section we will discuss cuts which address the quality of the reconstructed track, in the following we will simply refer this as the “track quality”. Assuming tracks are mostly continuous in clusters, i.e. only randomly missing a few clusters, the number of clusters is directly related to the momentum resolution of a track. Tracks with more clusters correspond to better PID and momentum resolution. Upward-going and downward-going tracks, at larger values of θ_{Lab} are

limited by the vertical space of the TPC. In these regions the track length is short and there are few clusters which are reconstructed. This leads to the low efficiency in these regions as discussed earlier in Sec. 1.8. A cut where tracks with the number of clusters $N_{cl} > 20$ are considered quality tracks. Later in Section ?? the exact choice of the number 20 is discussed in more detail.

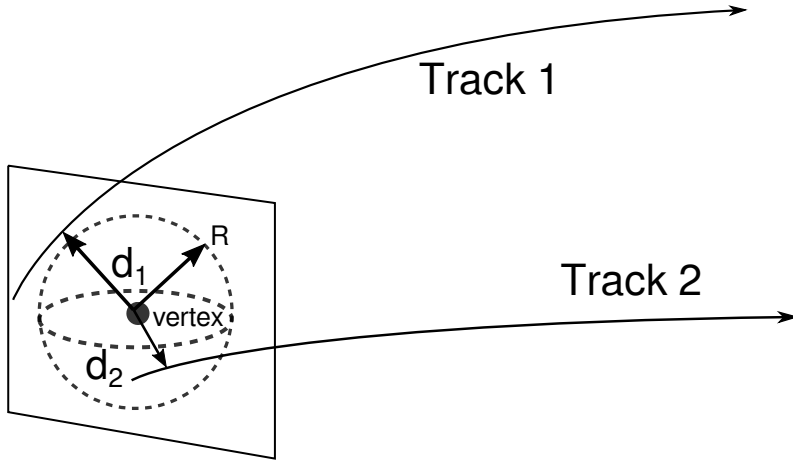


Figure 2.10: Distance to vertex for tracks.

For very long tracks, such as low momentum pions, which can make a complete circular path in the TPC, it can happen that the software incorrectly identifies the track as several separate tracks. This can happen due to discontinuities in the track due to missing hits from low energy loss, shadowing due to saturation, or possibly the software algorithm itself. Of course including all of the tracks would be counting the track several times over, and would lead to incorrect particle yields. The software will occasionally associate random disassociated clusters and construct a false track, or a so called “ghost track”. These type of tracks contribute to the background in the PID. In both of the situation of the false track or in the case of a split track the false track origin cannot be traced back to anywhere near the vertex of the event, and the distance-Of-Closest-Approach (dOCA) between the track and vertex is very large.

To reduce the number of false tracks, a simple cut on the dOCA can be used. The vector representing the minimum distance to vertex for each track can be calculated and its corresponding magnitude. We define the distance to vertex cut as a small sphere centered around the vertex

location with a some radius R . If the dOCA of a particular track $d_i < R$, the track is assumed to have originated from the vertex; tracks outside of the cut are thrown out of the analysis.

2.9 Angular Quality Cuts

Since the TPC does not have spherical symmetry, there are geometric constraints and considerations that effect the efficiency of track reconstruction. Most notably upward and downward-going tracks will have the shortest track length and will correspond to low regions of efficiency as seen in 1.8. The relevant geometries which determine these regions are the corners of the field cage. Figure 2.11 shows a cartoon drawing of the front of the field cage were the angles of each corner is given. Since the window to the field cage was slightly higher, the upper angles are slightly smaller than the lower angles. These angles are actually the same as the spherical ϕ angle, where the left and right, most efficient regions, correspond to $0^{\circ+24}_{-34}$ and $180^{\circ+34}_{-24}$. While the exact area of zero efficiency depends on polar angle θ_{Lab} , a clear cut off around these angles can be seen in Fig. 2.11 in the angular distribution of the measured tracks, where the experimental data was fitted with a Fermi distribution to find the inflection point of where the efficiency drops off significantly. The angular cuts applied to the data is listed by particle type in Table 2.5. The values are very similar to the simple calculation that was outlined above.

Particle Type	θ_{CM} cut	ϕ cut
π^+	$\theta_{CM} < 90^\circ$	$-35^\circ < \phi < 20^\circ \cap 157^\circ < \phi < 219^\circ$
π^-	$\theta_{CM} < 90^\circ$	$-40^\circ < \phi < 25^\circ \cap 158^\circ < \phi < 212^\circ$

Table 2.5: Angular cuts for each system and particle type

These regions can also be seen in the earlier discussion in the MC embedded efficiency in Fig. 1.33. We could of course include a larger region where the efficiency is small but not zero but it is good practice not to efficiency correct already small numbers with small efficiency values. The solid angle covered by the cut is written as,

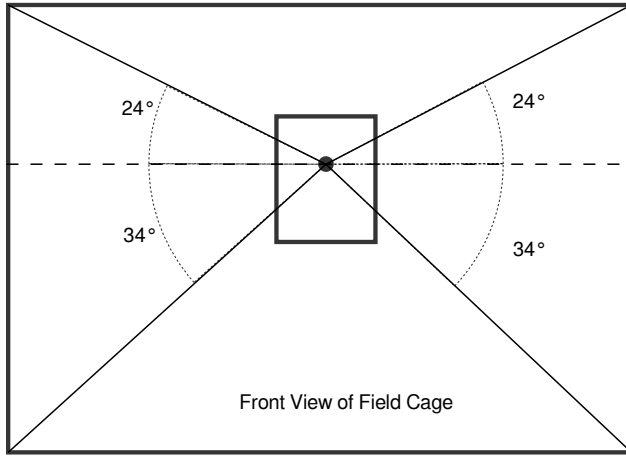


Figure 2.11: Rough Geometry of the TPC field cage.

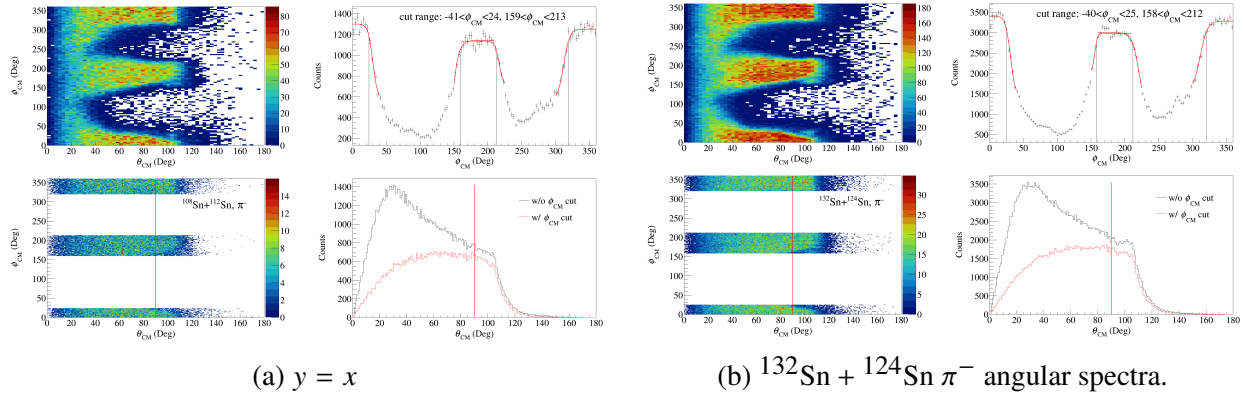


Figure 2.12: Three simple graphs

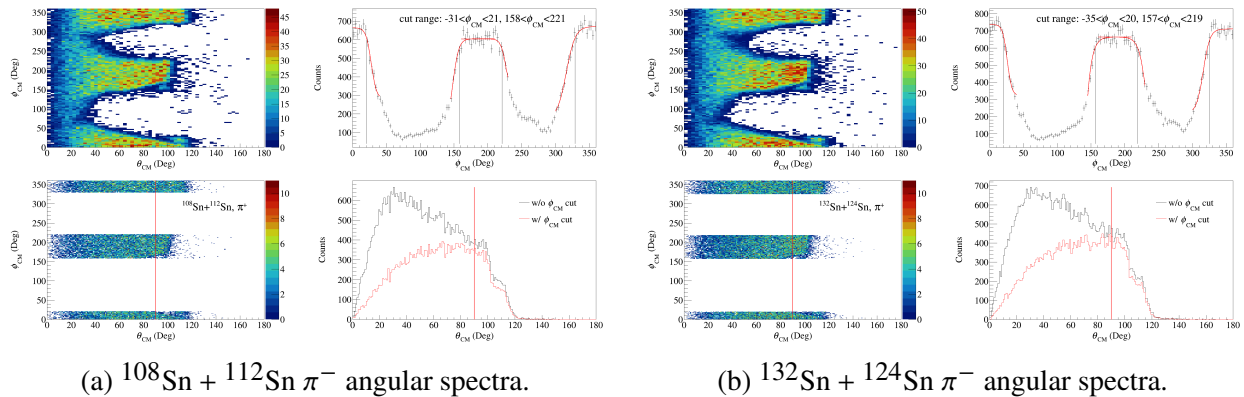


Figure 2.13: Three simple graphs

$$\Delta\Omega = \Delta\phi(\cos(\theta_1) - \cos(\theta_2)), \quad (2.6)$$

where $\Delta\phi = (\phi_2 - \phi_1)$ and $\theta_{1,2}$ are the θ angle cuts, in units of rad. The solid angle covered by the π^- cuts is 2.077 sr and for π^+ cuts 2.042 sr. Assuming the pion emission is isotropic, we multiply each observed pion by a correction factor, C_a , to correct for the full 4π angular coverage,

$$C_a = \frac{4\pi}{\Delta\Omega}, \quad (2.7)$$

for π^+ that is 6.15 and π^- 6.05. We assume the pion emission is isotropic for a couple of reasons. The symmetry of very central collisions is invariant with respects to any rotations. Also the mass of the pion is smaller than the nucleons mass and therefore collective motion leading to anisotropies would be small for the pion, i.e. most of the motion would be thermal. We also measured two systems $^{112}\text{Sn} + ^{124}\text{Sn}$ and its inverse $^{124}\text{Sn} + ^{112}\text{Sn}$. The forward emission in the $^{124}\text{Sn} + ^{112}\text{Sn}$ system is really the same as the backward emission of the $^{112}\text{Sn} + ^{124}\text{Sn}$ system and vice versa. It was shown for pions emitted in central collisions the forward and backward emission was the same [12], proving that at least for central collisions pions are emitted isotropically to a good approximation.

APPENDIX

APPENDIX

RUNS ANALYZED IN THIS DATA

System	#runs	Run numbers
$^{132}\text{Sn} + ^{124}\text{Sn}$	113	2841, 2843, 2844, 2845, 2846, 2848, 2849, 2850, 2851, 2852, 2855, 2856, 2857, 2858, 2859, 2860, 2861, 2875, 2877, 2878, 2879, 2880, 2881, 2882, 2883, 2884, 2887, 2888, 2889, 2890, 2891, 2892, 2893, 2894, 2896, 2898, 2899, 2900, 2901, 2902, 2903, 2904, 2905, 2907, 2914, 2916, 2917, 2919, 2920, 2921, 2922, 2924, 2925, 2926, 2927, 2929, 2930, 2931, 2932, 2933, 2934, 2935, 2936, 2939, 2940, 2941, 2942, 2943, 2944, 2945, 2946, 2948, 2955, 2956, 2958, 2959, 2960, 2961, 2962, 2964, 2965, 2966, 2968, 2969, 2970, 2971, 2972, 2973, 2975, 2976, 2977, 2978, 2979, 2980, 2981, 2982, 2983, 2984, 2985, 2986, 2988, 2989, 2990, 2991, 2992, 2993, 2997, 2999, 3000, 3002, 3003, 3007, 3039
$^{124}\text{Sn} + ^{112}\text{Sn}$	60	2542, 2543, 2544, 2546, 2547, 2548, 2552, 2553, 2554, 2555, 2556, 2557, 2558, 2559, 2560, 2562, 2563, 2564, 2565, 2566, 2567, 2568, 2569, 2570, 2571, 2572, 2573, 2574, 2575, 2578, 2579, 2580, 2581, 2582, 2583, 2584, 2585, 2586, 2587, 2588, 2589, 2590, 2591, 2592, 2593, 2594, 2595, 2596, 2597, 2598, 2599, 2600, 2601, 2617, 2618, 2619, 2620, 2621, 2622, 2623
$^{112}\text{Sn} + ^{124}\text{Sn}$	68	3059, 3061, 3062, 3065, 3066, 3068, 3069, 3071, 3074, 3075, 3076, 3077, 3078, 3080, 3081, 3082, 3083, 3084, 3085, 3087, 3088, 3089, 3090, 3091, 3092, 3093, 3094, 3095, 3097, 3098, 3102, 3103, 3138, 3139, 3140, 3141, 3142, 3143, 3144, 3145, 3146, 3148, 3149, 3150, 3151, 3152, 3153, 3154, 3155, 3156, 3157, 3158, 3159, 3165, 3166, 3167, 3168, 3169, 3170, 3171, 3172, 3177, 3179, 3180, 3181, 3182, 3183, 3184
$^{108}\text{Sn} + ^{112}\text{Sn}$	85	2272, 2273, 2274, 2275, 2276, 2283, 2284, 2285, 2286, 2288, 2289, 2291, 2310, 2311, 2314, 2315, 2320, 2322, 2323, 2324, 2325, 2331, 2332, 2333, 2334, 2335, 2336, 2337, 2340, 2341, 2362, 2363, 2368, 2369, 2370, 2371, 2372, 2373, 2374, 2375, 2378, 2379, 2380, 2381, 2382, 2383, 2384, 2385, 2386, 2387, 2388, 2389, 2391, 2392, 2393, 2394, 2395, 2396, 2397, 2398, 2399, 2400, 2401, 2402, 2429, 2432, 2433, 2434, 2437, 2438, 2439, 2440, 2442, 2453, 2461, 2462, 2463, 2501, 2502, 2503, 2505, 2506, 2507, 2508, 2509

Table .1: List of runs for the analysis.

APPENDIX

SECOND APPENDIX

BIBLIOGRAPHY

BIBLIOGRAPHY

- [1] M. Al-Turany, et al., The fairroot framework, *J. Phys.: Conf. Ser.* 396 (2). doi:10.1088/1742-6596/396/2/022001.
- [2] C. Höppner, et al., A novel generic framework for track fitting in complex detector systems, *Nucl. Instrum. Meth. A* 620 (2-3) (2010) 518–525. doi:10.1016/j.nima.2010.03.136.
- [3] W. Waltenberger, Rave—a detector-independent toolkit to reconstruct vertices, *IEEE Transactions on Nuclear Science* 58 (2) (2011) 434–444. doi:10.1109/TNS.2011.2119492.
- [4] H. Bichsel, A method to improve tracking and particle identification in tpcs and silicon detectors, *Nuclear Instruments and Methods in Physics Research Section A: Accelerators, Spectrometers, Detectors and Associated Equipment* 562 (2006) 154–197.
- [5] E. Gatti, et al., Optimum geometry for strip cathodes or grids in mwpc for avalanche localization along the anode wires, *Nucl. Instr. Meth. Phys. Res. A* 163 (1979) 83–92. doi:10.1016/0029-554X(79)90035-1.
- [6] S. Collaboraiton, Samurai dipole magnet field map (2020).
URL <https://ribf.riken.jp/SAMURAI/index.php?Magnet>
- [7] G. Van Buren, et al., Correcting for distortions due to ionization in the star tpc, *Nucl. Instrum. Meth. A* 566 (1) (2006) 22–25. doi:10.1016/j.nima.2006.05.131.
- [8] T. Isobe, et al., Application of the generic electronics for time projection chamber (get) readout system for heavy radioactive isotope collision experiments, *Nucl. Instrum. Meth. A* 899 (2018) 43–48. doi:10.1016/j.nima.2018.05.022.
- [9] D. Morrissey, B. Sherrill, *In-Flight Separation of Projectile Fragments*, Springer, Berlin, Heidelberg, 2004.
- [10] N. Fukuda, T. Kubo, T. Ohnishi, N. Inabe, H. Takeda, D. Kameda, H. Suzuki, Identification and separation of radioactive isotope beams by the bigrips separator at the riken ri beam factory, *Nuclear Instruments and Methods in Physics Research Section B: Beam Interactions with Materials and Atoms* 470 (2001) 562–570.
- [11] K. Kimura, T. Izumikawa, R. Koyama, T. Ohnishi, T. Ohtsubo, A. Ozawa, W. Shi-nozaki, T. Suzuki, M. Takahashi, I. Tanihata, T. Yamaguchi, Y. Yamaguchi, High-rate particle identification of high-energy heavy ions using a tilted electroe gas ionization chamber, *Nuclear Instruments and Methods in Physics Research Section A: Accelerators, Spectrometers, Detectors and Associated Equipment* 608 (2005) 608–614.
- [12] J. E. Barney, Charged pion emission from reactions with the srit time projection chamber, Ph.D. thesis (2019).
- [13] C. Cavata, M. Demoulins, J. Gosset, M. Lemaire, D. Hote, J. Poitou, O. Valette, Determination of the impact parameter in relativistic nucleus-nucleus collisions, *Physical Review C* 42 (4) (1990) 1760–1763.

- [14] L. Phair, D. Bowman, C. Gelbke, W. Gong, Y. Kim, M. Lisa, W. Lynch, G. Peaslee, R. de Souza, M. Tsang, F. Zhu, Impact-parameter filters for $^{36}\text{Ar} + ^{197}\text{Au}$ collisions at $e/a=50$, 80 and 110 mev, Nuclear Physics A 548 (1992) 489–509.